Structure and Magnetic Properties of New Be-Substituted Langasites $A_3Ga_3Ge_2BeO_{14}$ (A = La, Pr, Nd, Sm, Eu)

By

Arzoo Sharma

A thesis submitted to the

Faculty of Graduate Studies of the University of Manitoba

in partial fulfilment of the requirements of the degree of

Master of Science

Department of Chemistry

University of Manitoba

Winnipeg, Manitoba, Canada

Abstract

The langasites are a class of geometrically frustrated compounds with the formula $A_3XY_3Z_2O_{14}$ where A,X,Y,Z are cationic sites and site A is occupied by a magnetic ion. The interactions of the magnetic ions form a star shaped pattern called the Kagomé lattice. The langasites have been widely studied by the solid state community because of their functional properties such as piezoelectricity, multiferroicity, ferroelectricity, dielectricity and for use in the telecommunication industry. It was also realized that some langasite materials exhibit exotic magnetic ground states at low temperatures. A thorough understanding of their ground state is limited by the difficulty in synthesizing new members belonging to this series due to the formation of competing phases such as the garnets. In this study, four new magnetic langasites $A_3Ga_3Ge_2BeO_{14}$ (A= Pr, Nd, Sm and Eu) and a non-magnetic lattice standard $La_3Ga_3Ge_2BeO_{14}$ were synthesized. These were further structurally characterized by powder X-ray diffraction, Rietveld refinement and bond valence analysis. Further characterization of the low-temperature magnetism was done by performing magnetization, magnetic susceptibility (field cooled and zero field cooled) and heat capacity measurements. The low temperature spin dynamics were probed using muon spin resonance performed at TRIUMF (Vancouver) and elastic and inelastic neutron scattering measurements performed at the DCS (NIST) and D7 (ILL). From all the above measurements it can be concluded that the new Be langasites exhibit net antiferromagnetic interactions at low-temperatures with clear signs of diffuse scattering for $Nd_3Ga_3Ge_2BeO_{14}$ using inelastic neutron scattering measurements. There was no evidence of magnetic long-range ordering down to as low as 0.025 K. Based on the obtained measurements these new Be-langasite compounds can be classified as potential spin liquid candidates.

Acknowledgements

First and foremost I would like to thank Dr. Chris Wiebe for your constant encouragement and support. You were always there for me as a mentor and a friend. You believed in me even when I doubted myself and I cannot thank you enough for that. Not only did you help me succeed as a chemist, you also taught me how to deal with failure and that is a life skill I will always treasure.

I had the opportunity to work with some very talented group members at the Wiebe group. Harlyn, you are a brilliant scientist. Thank you for training me in everything from grinding samples to taking measurements and data analysis. I wish you lots of success in life. Alannah, Paul, Micaela, Abigail, Cole, Simeone, Kanisha, Avi, Brenden, Meghan and Kelsey, working with you was a pleasure. I was also lucky to have the most supportive office mates Mimi Luong and Jonathan Challis, thank you guys.

I would like to thank my committee members Dr. Can-Ming Hu, Dr. Mario Bieringer and Dr. Peter Budzelaar. Thanks to Mario for his guidance and providing valuable insight into my projects. A special thanks to Joey for all the successful collaborations. It was a great learning experience and I look forward to many more collaborations in the future.

Last but not the least I could not have done this without the unconditional love and encouragement from my family and friends, thank you for being there for me.

Table of Contents

List of Figures

List of Tables

Chapter 1

Introduction

Part I

1.1 Magnetism in everyday life

Over the years, magnetic materials have impacted different aspects of human life starting from the marine compass to enhanced burglar alarms, microphones, and electric bells. Magnetic materials are currently being used to enhance the storage capacity in hard drives and in making energy efficient electronic devices like laptops and highly compact smart phones.

In the future, superconducting magnetic materials can be used to bring down the cost of medical services like MRI (Magnetic Resonance Imaging) and NMR (Nuclear Magnetic Resonance spectroscopy). Thus, there is a need for further research and discovery of new magnetic materials which will enable one to explore the wide possibilities that are beyond reach at this time.

1.2 Geometric frustration

Geometric frustration is a phenomenon observed in certain magnetic materials due to the alignment of their spins. It results when the lattice geometry inhibits the formation of an ordered spin configuration at low temperatures. Thus the spins are unable to satisfy their local constraints and become frustrated [1]–[5]. The complex behaviour of antiferromagnetic interactions can be illustrated by three spins on a triangular lattice. At any given moment when two spins align anti parallel to each other, the third spin cannot lie antiparallel to the already aligned spins and thus is frustrated. Instead of forming a single ground state it usually forms degenerate multifold of ground states. This means that at any given time the system can exist in one of the six combinations of spins on the three vertices where all these states have equal energy. Another

example of geometric frustration can be observed in the case of a tetrahedron which is comprised of four edge-sharing equilateral triangles. In this case, only two neighbouring spin interactions can be satisfied at a time leading to geometric frustration (figure 1.1) [1]–[5].

The degenerate multifold ground states, which are a result of lattice geometry, leads to magnetic analogs of liquids and ices in solid state materials like the spin liquids.

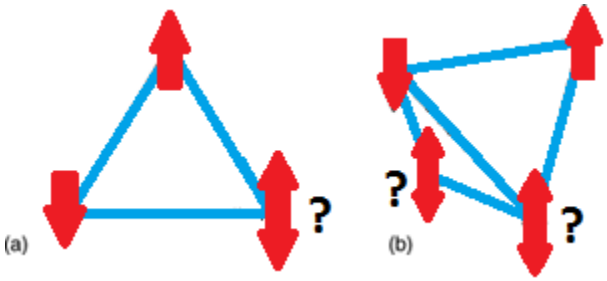

Figure 1.1 The rise of geometric frustration in 2-D (a) and 3-D (b) lattices due to the alignment of Ising spins in antiferromagnetic ordering [5].

1.3 Spin Liquid

When the zero point fluctuations are strong enough to prevent magnetic long range order because of the disordered state of spins, the system is said to exist in a spin liquid state. In these states the spins are highly correlated but do not order even when the temperature approaches 0 K [6]. The spins fluctuate strongly when being cooled and lead to the formation of a dynamic spin state which can be compared to liquid states of matter. At any given moment the spins exhibit short range ordering. This ordering, however, is not static. As the temperature is lowered, the thermal fluctuations decrease and the spins cannot flip-flop between different states anymore. Thus, either freezing of spins or magnetic ordering takes place. When the spins in question are small, however, fluctuations as a result of the quantum mechanical uncertainty principle persists down to low temperature. Experimentally, quantum spin liquids have certain features that separate them from other types of frustrated materials. Some of the features include no magnetic ordering down to 0 K, persistent spin fluctuations which can be seen by neutrons scattering, Nuclear

Magnetic Resonance (NMR) and Muon Spin Relaxation (MSR) measurements, a T^2 dependence on heat capacity for 2D quantum spin liquids and a negative Curie-Weiss temperature with a large magnitude [7]. The above mentioned experimental features have been observed in some Kagomé systems [8] and thus materials with a Kagomé network are promising quantum spin liquid candidates.

1.4 The Kagomé Network

The term Kagomé arises from a Japanese weaving pattern and resembles a star pattern as shown in figure 1.2. The corner sharing triangular lattice is stacked in two dimensions and the spins are positioned on the corners of these triangles.[1], [5], [9].

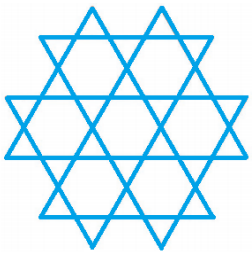

Figure 1.2 An ideal star shaped Kagomé lattice (right) [1], [5] .

Herbertsmithite ($ZnCu_3(OH)_6Cl_2$) is one of the most widely studied Kagomé networks which has shown evidence of a possible quantum spin liquid state [10], [11]. The copper atoms in a Herbertsmithite lie on the corners of the Kagomé triangles. Low temperature physical property measurements show no signs of magnetic ordering down to 0.050 K and a high coupling constant [12]. Some of the other compounds having the Kagomé lattice that have been previously studied are the Jarosite family. Two members of this family; $KFe_3(OH)_6(SO_4)_2$ and $KCr_3(OH)_6(SO_4)_2$ [13], have an ideal Kagomé lattice and are well characterized. Another class of compounds with a Kagomé like lattice is volborthite $Cu_2V_2O_7(OH)_2.2H_2O$ [14] with S=1/2 that has been extensively studied. All of these systems are Heisenberg (3 dimensional vector spins) spin Kagomé antiferromagnets. There are not many examples of chemically ordered Ising (discrete spins) or XY (planar vector spins) Kagomé lattices (figure 1.4) [15]. Properties of Ising and XY

spin systems can be very different from Heisenberg since the spin orientation is now restricted and this can give rise to interesting properties that have not been observed before. Thus exploring members with such lattices is important [16]. Langasite materials can be promising members for this study.

1.5 Langasites

The langasites are a class of geometrically frustrated compounds with the formula $A_3XY_3Z_2O_{14}$ where A,X,Y,Z are cationic sites and the magnetic ion occupies site A in the structure. They have been widely studied by the solid state community because of their functional properties such as piezoelectricity [17], multiferroicity [18], ferroelectricity, dielectricity [19] and for use in the telecommunication industry [19].

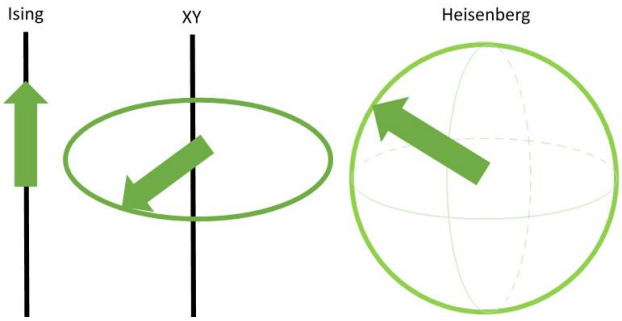

Figure 1.3 Comparison of Ising, XY and Heisenberg spins. (adapted from [15].)

Magnetic ions (Ising spins, figure 1.3) occupying the A site in langasites are arranged on the Kagomé network.[20], [21] Mill *et al.* [19] have identified over a hundred compounds belonging to this group and many more are reported by other authors [19], [22], [23]. $Pr_3Ga_5Si_2O_{14}$ (PGS) and $Nd_3Ga_5Si_2O_{14}$ (NGS) are two extensively studied langasites for their spin liquid like properties. Previously reported Sm langasites include $Sm_3Ga_{2.63}Al_{2.37}SiO_{14}$ [24] and $Sm_3Ga_2Al_3SiO_{14}$ [25]; both of these Sm langasites could be precisely prepared with the presence of a garnet impurity phase.

The synthesis and study of new members belonging to the langasite series is necessary to understand their low temperature magnetic properties. This thesis reports the synthesis of five

(four magnetic and one non-magnetic) new compounds belonging to the langasite family. By making a careful substitution on the Y site and the Z site, the overall size of the lattice was reduced. The reduced lattice size results in stronger exchange interactions and thus can provide more information about the ground states of these materials [6].

1.6 Magnetic order

The response of the material in an applied external field can be classified into the following types.

1.6.1 Paramagnetism

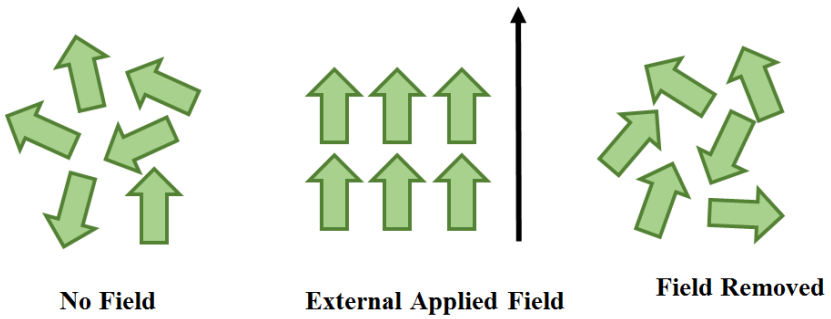

Figure 1.4 Arrangement of spins in no field (left), external applied field (middle) and after the removal of applied field (right) in the case of paramagnetism.

Paramagnetic materials lower their energy by moving into a magnetic field so the magnetic susceptibility is greater than zero ($\chi > 0$).They have a magnetic moment that can align itself in the direction of the applied field but the order of moments is lost as soon as the field is removed because of the thermal motion of electrons [26], [27].

1.6.2 Diamagnetism

Diamagnetic materials are characterized by a negative magnetic susceptibility ($\chi < 0$). The magnetization in these materials is in the opposite direction of the applied field which is governed by Lenz's law [27]. Lenz's law states that "An induced current is always in such a direction as to oppose the motion or change causing it" [26]. Thus it leads to a negative magnetic susceptibility in the material. Diamagnetism is a weak form of interaction and although it is present in all materials, it is not very evident as it is dominated by other stronger interactions [26]–[28].

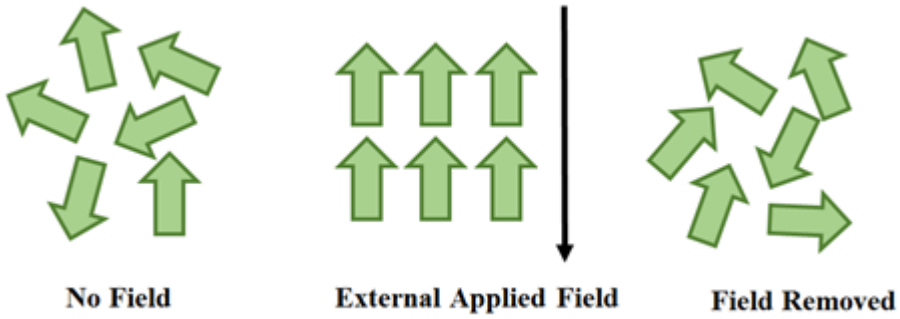

Figure 1. 5 Arrangement of spins in no field (left), external applied field (middle) and after the removal of applied field (right) in the case of diamagnetism.

1.6.3 Ferromagnetism

Ferromagnetic materials have a strong magnetic moment which is aligned in a particular direction even in an absence of external field beneath the Curie temperature (T_C). In the presence of external field the moments tend to align parallel to the field.

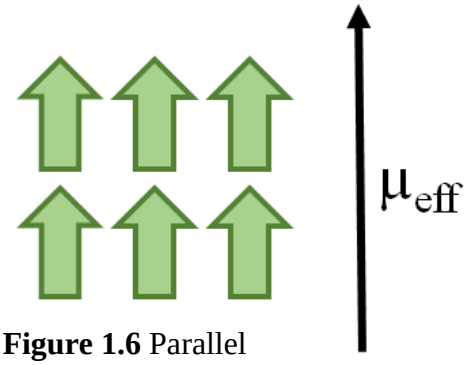

Figure 1.6 Parallel arrangement of magnetic moments leading to an effective magnetic moment.

1.6.4 Antiferromagnetism

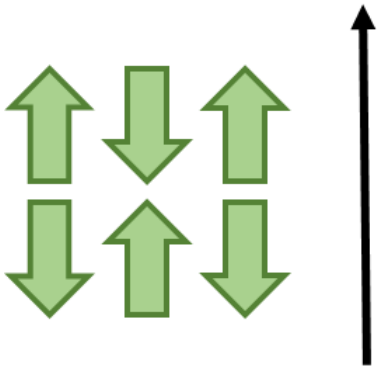

Figure 1.7 Anti-Parallel arrangement of magnetic moments leading to zero effective magnetic moment in the case of antiferromagnetism.

Antiferromagnetism is a type of magnetism when the spins are aligned antiparallel to each other and there is no net moment observed in the material. The antiferromagnetic nature is exhibited at low temperatures and above a certain temperature the spins become disordered (called the Néel temperature). Above the Néel temperature the material exhibits paramagnetism [27]. At the Néel temperature, the magnitude of the exchange energy is greater than the thermal energy and thus the spins align antiparallel to each other. Below the Néel temperature, the magnetization depends on the orientation of field and approaches zero as the temperature is decreased further. At this stage, the spins align in an ordered state with no net moment [26].

1.6.5 Ferrimagnetism

Ferromagnetism is a special case of antiferromagnetism where the spins align antiparallel to each other but the magnitude of the moments is different. This coupling between spins with unequal moments leads to an ordered magnetic state with overall magnetization known as ferrimagnetism [28].

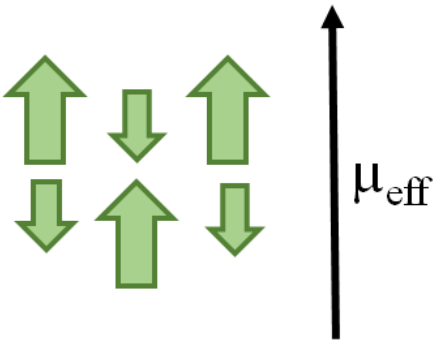

Figure 1.8 Antiparallel arrangement of the magnetic moments of different size leading to an effective magnetic moment

Ferrimagnetic materials can thus exhibit spontaneous magnetization even in an absence of an applied magnetic field [26].

Introduction

Part II

1.7 Synthesis

With the advancement in technology, there is an increased demand for the synthesis of new materials, understanding their properties and using them to enhance the existing technology. Synthesizing new functional materials effectively with the use of minimum resources has been challenging. Some of the commonly used methods are film deposition [29], sol-gel [30] , co-precipitation [31], precursor [32], microwave synthesis [33], combustion synthesis [34] high pressure [35] and chemical vapour deposition [36]. Doing this on a large scale can be achieved by finding the optimal synthesis conditions in the laboratory.

The shake and bake (or heat and beat) method of synthesis is the most common one in solid state chemistry. It involves mixing non-volatile reactants, compressing them and heating them until they are completely reacted to form a desired phase. High temperatures are required for the ions to migrate to a new sites and form a different lattice. A limitation of the method is that compounds that are volatile at high temperature cannot be reacted as they evaporate from the system. Since diffusion is the driving force, it is difficult to control kinetically stable products.

1.8 Crystal Growth

A crystal consists of atoms of a material arranged in an orderly repeating pattern which extends in all three dimensions. Different methods of crystal growth are used widely. Depending on the physical state of the material during the growth the methods can be broadly classified as vapour phase growth, solution growth, solid state growth and melt growth [37]. The floating zone technique (FZ) is a type of melt growth method where the material is heated to very high

temperatures and cooled in order to form crystals. The FZ technique has some advantage over the other melt growth methods (for example it does not require the use of any crucible which greatly reduces the chance of sample contamination or reaction between crucible and sample) [38]. Langasites are in general incongruently melting crystals. This means that even though same amount of heat is being supplied to the crystal, some parts of the material will melt faster than the other. The melting is not homogenous which makes the crystal growth process difficult.

1.9 X-Ray Diffraction

X-rays are high energy electromagnetic radiations with energies between 200 eV to 1 MeV. X-ray diffraction has been modified over the years to serve different purposes in the scientific community like identifying and characterising materials, understanding the atomic structure, stereochemistry and so on [39], [40].

X-rays typically interact weakly with matter and thus the diffraction can be restricted to single scattering. This means that it can be assumed that the rays scatter just once from the sample and a scattered wave will not scatter from the said sample more than once (this is called the kinematic approximation). Also, the incoming and outgoing waves are treated as plane waves [41]. The Braggs came up with the description for the waves which is used nowadays [39], [41]. These waves are considered plane waves and the wavelength of x-rays have the same magnitude as the distance between the atoms of the unit cell. The diffraction of rays from matter gives rise to constructive and destructive interferences. The constructive interference from all the layers results in sharp maxima in the diffraction called Bragg peaks. The Braggs stated a law which

relates the occurrence of constructive interference with the angle of incidence and the wavelength of incident light (called Bragg's law).

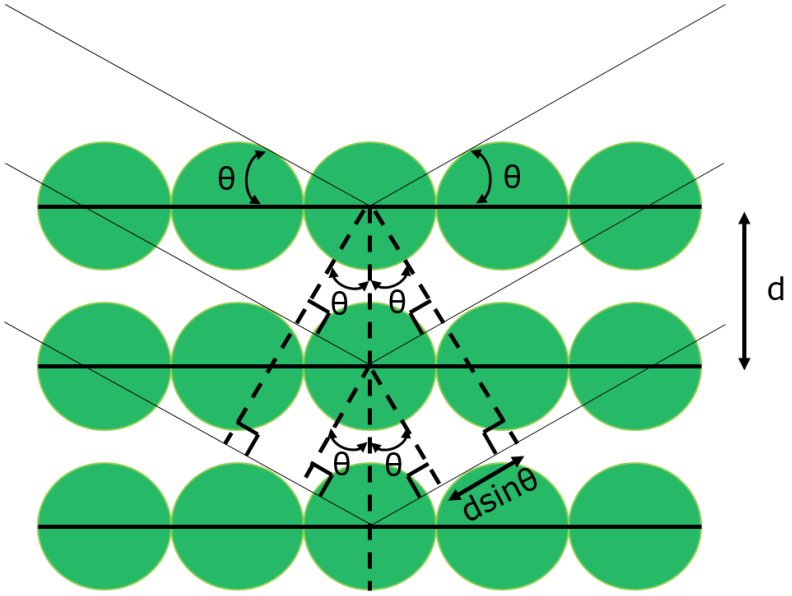

Figure 1.9 Schematic illustration of Bragg's law.

The interference pattern follows Bragg's law

$$2dsin\Theta = n\lambda \quad (1.1)$$

Where d is the spacing between the Bragg planes, Θ is the angle between the x-rays and the specific plane of reflection, λ is the wavelength and n is an integer. The position and intensity of the Bragg peaks help in determining the structure of the compound [42]. Bragg's law provides information of plane separations and thus enables the determination of unit cell metrics. The atomic structure is obtained through a Fourier transform of the intensity pattern.

1.9.1 Powder Diffraction

Powder diffraction is an important tool in solid state chemistry for crystal structure identification and refinement. An accurately obtained powder diffractogram can provide detailed information about the sample including structure (atomic positions), particle size, homogeneity of particle size and lattice parameters. For samples containing more than one phase, the different phases can

be identified quantitatively [43]. The diffractometer used in this study was the Huber Image Plate Guinier camera G670 with $CuK_{\alpha 1}$ radiation with a transmission geometry.

1.10 Rietveld Refinement

The Rietveld refinement method is a least square regression to obtain a good fit between the experimental diffraction pattern obtained using the x-ray diffractometer and the calculated pattern using a trial structure. Different parameters such as the atomic coordinates, thermal parameters and occupancies are refined to enhance the fit between the two data sets.[43]–[46]. A diffraction pattern obtained from a powder sample consists of different peaks as a function of 2Θ in case of x-rays and a velocity function in case of time of flight neutrons.

At any given step, if the observed intensity is $y_{o,i}$ and background is $y_{b,i}$, the calculated profile intensity is given by $y_{c,i} = y_b + \Sigma y_{\mathbf{h}}$ where **h** = hkl Bragg reflections [44].

There are certain criteria used to determine the best fit between calculated and experimental patterns. The different factors compare the obtained and the theoretically calculated data and helps in determining the goodness of fit.

The first one is the conventional R-factor and is given by

$$R_f = \frac{\Sigma j \, |\sqrt{I_{obs,j}} - \sqrt{I_{calc,j}}|}{\Sigma j \, |\sqrt{I_{obs,j}}|} \qquad (1.2)$$

The Bragg R-index factor provides a comparison of integrated intensities. R_B is calculated by assigning the actual observed intensities obtained by scanning at each step to the Bragg intensities. The assignment is made based on the calculated intensities because of the lack of real integrated intensities. It is given by

$$R_b = \frac{\Sigma j\ |I_{obs,j} - I_{calc,j}|}{\Sigma j\ I_{obs,j}} \quad (1.3)$$

The profile factor is given by

$$R_p = \frac{\Sigma j\ |y_{obs,j} - y_{calc,j}|}{\Sigma j\ y_{obs,j}} \quad (1.4)$$

The weighted profile factor R_{wp} is important and most reliable as the numerator is the residual that is minimized in the least squares procedure. It is given by

$$R_{wp} = \sqrt{\frac{\Sigma j\ wj(y_{obs,j} - y_{calc,j})^2}{\Sigma j\ wj(y_{obs,j})^2}} \quad (1.5)$$

The statistically expected R factor R_e is given by

$$R_e = \frac{N - P + C}{\Sigma j\ wj(y_{obs,j})^2} \quad (1.6)$$

Where N = number of observations, j = experimental powder profile, P = number of parameters refined, and C = number of constraints.

Lastly, the goodness of fit indicator χ^2 is given by

$$\chi^2 = \left(\frac{R_{wp}}{R_e}\right)^2 \quad (1.7)$$

1.11 Bond Valence Analysis

L. Pauling in 1929 came up with the valence principle which defines the atomic valences of an atom as the sum of valences of all bonds to that atom.[47]

There are certain assumptions and theorems that are made for atoms for valence bond theory

1. All atoms, whether they are bonded to other atoms or not are assumed to be spherical.
2. The charge on atoms is considered zero in valence bond theory.
3. Every atom contributes the same number of valence electrons to the bond and this number is known as the bond valence for the atom.
4. The ionization energy difference between the core and valence shell electrons is assumed to be large.
5. In order to form bonds, the excited states of the atoms are expected to lie at a much higher gap than the ground state.
6. The bonding and nonbonding electrons might both be present in the valence shell.
7. For two bonded atoms, the bond is localized between them. [48]

Bond Valence Analysis of a compound is the estimation of oxidation states using theoretical bond distances (literature based) and actual bond distances. The bond valence is given by

$$\text{B.V.} = e^{\left(\frac{R_O - R}{b}\right)} \qquad (1.8)$$

where R is the length of a bond between the two given atoms and R_o and b are called the bond valence parameters. Bond length and bond valence are related such that the product of bond valence and average bond length is constant for the same bonds [47]. Bond valence analysis is important as experimental atomic valences can be calculated. The obtained experimental valences can be compared to the theoretical numbers. If an inconsistency is discovered between the two numbers this may indicate that the structure is either not correctly determined or there are discrepancies in the interpretation of the said structure. It can also be used to account for

undetected hydrogen. This can come in handy especially when dealing with new structures. Bond valence analysis can be used to estimate site mixing for ions with different oxidation states and can also be used to analyze the structural chemistry of lone pair cations and hydrogen bonding.[49]

1.12 Magnetic Susceptibility

The magnetic susceptibility of a compound is defined as its degree of magnetization in an applied magnetic field. The magnetic susceptibility per unit volume is given by

$$\chi = \frac{\mu_o M}{B} \tag{1.9}$$

Where μ_o is the permeability of free space, M is the magnetic moment of material per unit volume and B is the magnetic field intensity [50] [51].

1.12.1 Field cooled vs. zero field cooled

The magnetic susceptibility measurements can be performed in two settings, field cooled and zero field cooled. In the field cooled setting, the field is applied at a high temperature and the sample is cooled to the base temperature. The data is collected as the temperature is raised from the base back to room temperature. In case of a zero field cooled run, the sample is cooled to the base temperature in the absence of field, the field is turned on at the base temperature and the data is collected as the temperature is raised. In both cases the effect on the magnetic susceptibility of the sample is determined as a function of temperature for a certain field.

1.12.2 Curie-Weiss Law

The magnetic susceptibility in the presence of an external field as a function of temperature is described by the Curie-Weiss Law.

$$\chi = \frac{C}{T - \theta} \tag{1.10}$$

where χ is the molar magnetic susceptibility, C is a constant known as the Curie constant, T is temperature in K and Θ is the Weiss temperature. A plot of 1/χ vs. temperature is known as a Curie-Weiss plot and ideally it should be linear if the Curie-Weiss law is obeyed. In antiferromagnets, magnetic moments of atoms align anti-parallel to produce a strong magnetic effect and the Curie Law becomes $\chi = C/(T+T_N)$, where T_N is the Néel temperature. Above Neel temperature T_N, the thermal energy can overcome the interaction induced order. The magnetic order vanishes and the material behaves like a simple paramagnet. In ferromagnets, T_c is known as the Curie temperature, and in antiferromagnets as the Néel temperature T_N. Another parameter that can be obtained from the Curie –Weiss fits is the magnetic moment of the magnetic ion. The magnetic moment is given by the relation (CGS units).

$$C = \frac{\mu_{eff}{}^2}{8} \tag{1.11}$$

1.12.3 Saturation of Magnetic Moment

The magnetic moments of a material are said to be saturated when the increase in an external magnetic field cannot increase the magnetization of the material any further. When an external magnetizing field H is applied to the material, it penetrates the material and aligns the magnetic moments parallel to the applied magnetic field. This alignment of moments leads to the formation of an internal magnetic field. As the strength of the external field is increased, the number of aligned magnetic moments increases which leads to a stronger internal magnetic field. As the external magnetic field is increased gradually, a point is reached when any further

increase in the external field cannot align any more moments and the magnetic moments are said to be saturated. For magnetic materials, below T_C, when a magnetic field is applied, the magnetization will increase to a point and plateau after. This is called saturation magnetization [28].

1.12.4 Brillouin Function

The Brillouin Function is a function used to describe the magnetization of an ideal paramagnet by determining its spin state. This is achieved by varying the applied magnetic field while keeping the temperature constant.

The Brillouin function is given by

$$B_J(x) = \frac{2J+1}{2J}\coth\left(\frac{2J+1}{2J}x\right) - \frac{1}{2J}\coth\left(\frac{x}{2J}\right) \tag{1.12}$$

$$\text{where} \qquad x = \frac{g_J \mu_B J B}{k_B T}$$

The behaviour of the Brillouin function is similar for all values of J. In terms of x, it increases as long as the value of x is small and reaches saturation for large x. Thus the magnetization increases with field for small fields but as the field is increased it reaches a saturation magnetization given by $N\mu_H = Ng\mu_B J$ where N is the number of atoms per unit volume and μ_H is the maximum moment of each atom in direction of H [52]. This corresponds to the maximum possible alignment of moments with the external field.

1.12.5 Crystal Fields

The source of magnetism in rare earth compounds is the 4f shell with unpaired electrons with a localized wavefunction. The rare earth ions thus act like free ions where the ground states can be given by Hund's rules. At room temperature the lowest multiplet is occupied (J= L ± S) because of the strong spin orbit coupling leading to the separation of multiplets [53] .

These rare earth ions experience an electric field with very high intensity from the neighbouring ions because of their valence electrons. This field is called the crystal field. The interaction of paramagnetic ions with crystal fields can lead to two effects. The first one is the inability of the states to be described by their **J** because of the breaking up of the coupling of **L** and **S.** The second one is the splitting of degenerate 2L+1 sublevels for a given L. Because of the splitting, the contribution of orbital motion to the magnetic moment vanishes [54]. The quenching of the orbital angular momentum in addition to the anisotropic charge distribution lead to interesting properties in rare earth ions [53].

1.13 Heat Capacity

Heat capacity is the amount of heat required by a substance to change its temperature by 1 K or deg C.

$$C = dQ/dT \tag{1.13}$$

The total heat capacity is a combination of the lattice heat capacity and magnetic heat capacity. The heat capacity due to the magnetic contribution was obtained by subtracting the lattice contribution of the non-magnetic analog $La_3Ga_3Ge_2BeO_{14}$. $La_3Ga_3Ge_2BeO_{14}$ is isostructural to the $A_3Ga_3Ge_2BeO_{14}$ (A=Pr, Nd, Sm, Eu) and thus provides a good lattice match.

$$3La_2O_{3\,(s)} + 3Ga_2O_{3(s)} + 4GeO_{2(s)} + 2BeO_{(s)} \longrightarrow 2La_3Ga_3Ge_2BeO_{14\,(s)}$$

1.13.1 Schottky Anomaly

For a system with multiple degenerate electronic levels, a broad maximum is observed in the heat capacity which is called the Schottky anomaly [55].

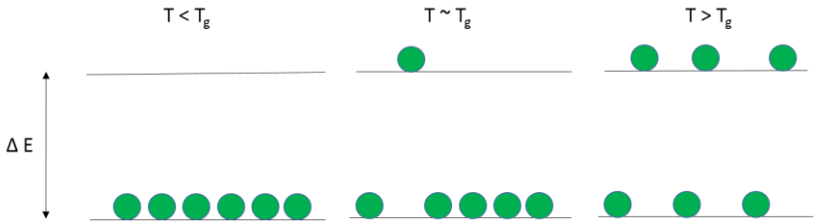

Figure 1.10 Two discrete energy levels separated by energy gap ΔE (Adapted from [89]).

A Schottky anomaly is different than the first and second order transitions. The anomaly is observed when there is a transition between discrete energy levels, where the spacing between the levels can be determined and they direct the behaviour of a system. At high temperatures, the energy scale of the excitations is very large. At low temperatures, however, there is not enough energy for the thermal excitations to overcome the energy barrier (low temperature states are improbable) and thus it gets difficult for the electrons to transition to the next level.

1.13.2 Hund's Rules

A graph can be plotted with C/T vs. T for a heat capacity measurement. The obtained curve can be integrated to determine the value of entropy for a temperature range of 1.8K to 300K.

$$S = \int \frac{Cp}{T} \mathrm{dT} \tag{1.14}$$

The obtained entropy can be used to find the value of total angular momentum J using the following relation.

$$\Delta S = R \ln(2J + 1) \tag{1.15}$$

The total angular momentum can be calculated from the vector sum of spin and orbital moments [41] The calculations can be carried out according to the Hund's rules. Hund's rules state [41]:

1. The spins of the electrons are arranged such that the maximum values of S consistent with Pauli's principle is achieved.
2. The quantum numbers m_l have to be chosen so that L is maximized.
3. J = L-S when the shell is less than half filled and L+S if more than half filled.

   For example, the electronic configuration of Sm^{3+} can be written as [Xe] $4f^5$. It contains five electrons in the valance shell. So S equals 5/2. Also L is the sum of orbital moments and is equal to 5.

   So J = L-S = 5 – 5/2 = 2.5

1.14 MuSR (Muon Spin Resonance)

The μSR technique has been used widely in the past to understand spin dynamics in different systems. When it comes to geometrically frustrated systems, μSR and neutron scattering measurements complement each other to provide a better understanding of the interactions. A dynamic state has been successfully realized in some geometrically frustrated systems using μSR. Thus μSR can be considered an important technique to study frustrated materials with quantum spin fluctuations. μSR is the study of the interactions of the muon spin dynamics when they interact with the spins of a material and decay [56]. The technique is named so in order to draw an analogy to the techniques like Nuclear Magnetic Resonance (NMR) [56].

1.14.1 Measurements using Muons

In order to perform measurements, the muons are implanted in the sample of interest. Polarized muons that have just enough energy to stop within the sample and not pass it are planted in the samples. Due to momentum conservation, a pion decaying at rest will result in muons and neutrinos with opposite momentum with respect to that of the pion. This means that the muon and muon neutrino will have opposite spin and since they form the muon beam, the beam will be polarized. The spin polarized muons, after getting planted in the sample, are monitored for the polarization of the muon as a function of time. This provides information regarding the local spin environment at each site where the muon is planted [57].

There are different ways to do μSR depending on the orientation of applied field [56]–[58].

1. ZF (Zero Field) μSR

The zero field relaxation technique is used for materials exhibiting weak magnetism. It is also a useful tool when looking for magnetic ordering. In this relaxation technique, the magnetic properties of the materials are probed without an applied external field.

There are two features in this technique that signify magnetic order. The first is the emergence of oscillations in the sample and the second one is the emergence of a baseline at long times below which the spectra does not relax.

2. LF (Longitudinal Field) μSR

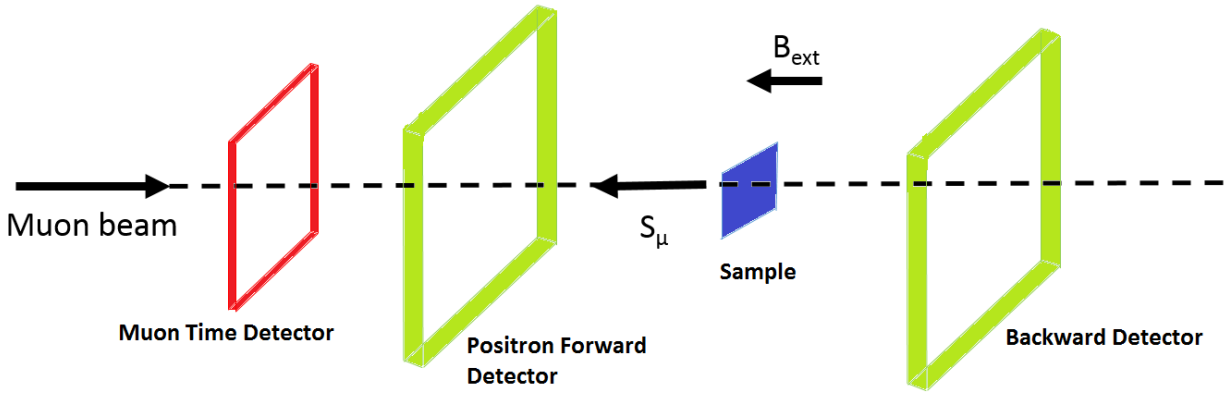

Figure 1.11 Longitudinal field orientation of applied field for μSR measurements [70].

The longitudinal field measurements are used to probe the spin dynamics of materials. It takes place in the presence of an applied external field which is parallel to the initial direction of the muon spin polarization. The time evolution of muon polarization is measured along the original direction of the field.

3. TF (Transverse Field) μSR

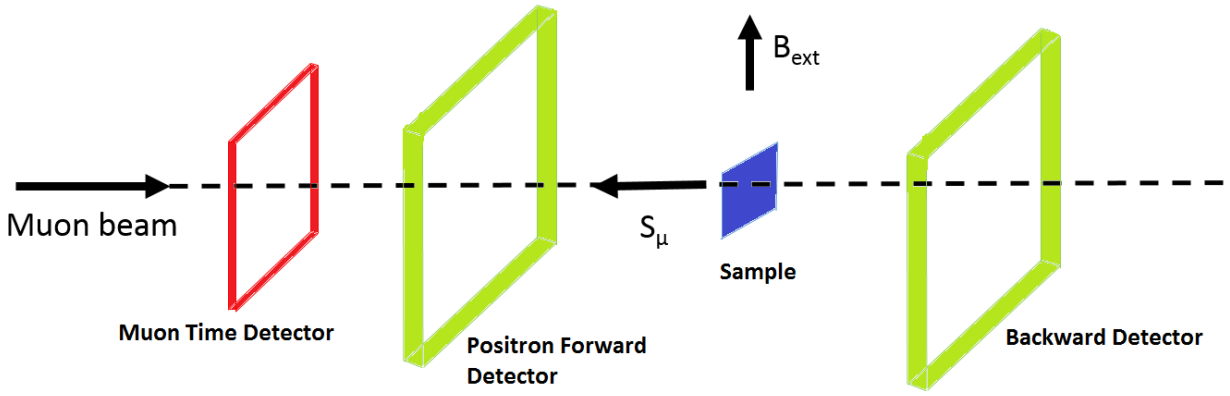

Figure 1.12 Transverse field orientation of applied field for μSR measurement [70].

In TF, an external field is applied perpendicular to the direction of muon polarization. The asymmetry function in an applied transverse field with muons stopped in an entirely inert sample

would be a cosine. In a sample, the cosine have a different frequency which would be expected in the applied field, and is modulated by a relaxing envelope dependent on the physics of the system being probed typically, and R(t) is some function describing the relaxation. In a magnetic system, the transverse field is small relative to the internal fields in the sample. TF measurements are analogous to a Knight shift in NMR. Sometimes the internal field can be changed by the magnetization of the material. This is accounted for carrying out the vector sum of the internal fields and applied field. TF geometry is also used to probe superconductivity as type II superconductors enter a mixed state in an applied field below their critical temperature.

1.15 Neutron Scattering

Neutron scattering is a technique where interactions of neutrons with the sample is used to understand the properties of that material. Currently, neutron scattering techniques are used not just in chemistry and physics but in other areas like environment, pharmaceutical, healthcare, nanotechnology and information technology [59].

"If Neutron did not exist, it would need to be invented"

- Bertram Brockhouse

1994 Nobel Laureate in Physics

1.15.1 Principle of Neutron Scattering

Neutron scattering techniques are used to understand the structure and dynamics of a system. Neutrons are sub atomic particles which can penetrate a material deeper than electromagnetic x-rays without getting deflected by the electron cloud of the materials. Also the interaction of neutrons with the nucleus is via nuclear forces which are short ranged, on the order of few Femtometers (1 Femtometer = 1.0×10^{-15} m) and with unpaired electrons via a magnetic dipole

interaction [60]. The neutron scattering from the whole material can be understood by looking at one nucleus at a time. The scattering of a neutron from a nucleus can be described in terms of the nuclear cross section [60]. The neutron scattering cross section of a system is the extent to which it can scatter neutrons when an effective area is exposed to the neutron beam and is given by [61]

$$\sigma = \frac{1}{\Psi}\ number\ of\ neutrons\ scattered\ per\ second \qquad (1.16)$$

Where σ is the neutron scattering cross is section and Ψ is the flux of neutron beam. It is measured in barns where 1 barn = $10^{-28}m^2$. When the neutron interacts with the material within this cross section, it gets scattered. [60].

1.15.2 Elastic and Inelastic Neutron Scattering

Neutron scattering is being used for different types of studies. Some of the studies include elastic scattering which is used to study the structure and arrangement of atoms in a structure, inelastic scattering which provides information about the dynamics of the material, small angle neutron scattering which is used to study structures of polymers and colloidal solutions and reflectometry which probes layered materials and interfaces [62].

Elastic and inelastic scattering can be distinguished based on the momentum and energy transfer.

If 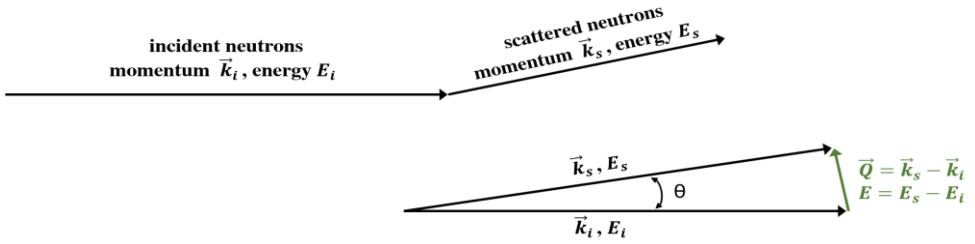

the

Figure 1.13 Comparison of energy and momentum transfer for elastic and inelastic neutron scattering [108].

momentum and energy of incident neutron is denoted by $\mathbf{k}_i$, E_i respectively and for scattered by

$\mathbf{k}_s$, E_s, the momentum transfer will be given by scattering vector $Q = \mathbf{k}_s - \mathbf{k}_i$ and energy transfer will be $E = E_s - E_i$. When there is a change in momentum but no change in energy, it is called elastic scattering and when both momentum and energy change it is called inelastic scattering [63].

Chapter 2

Experimental Techniques

2.1 Synthesis

The powder samples of the langasites $A_3Ga_3Ge_2BeO_{14}$ (A=La, Pr, Nd, Sm and Eu) were synthesised using standard solid state reactions.

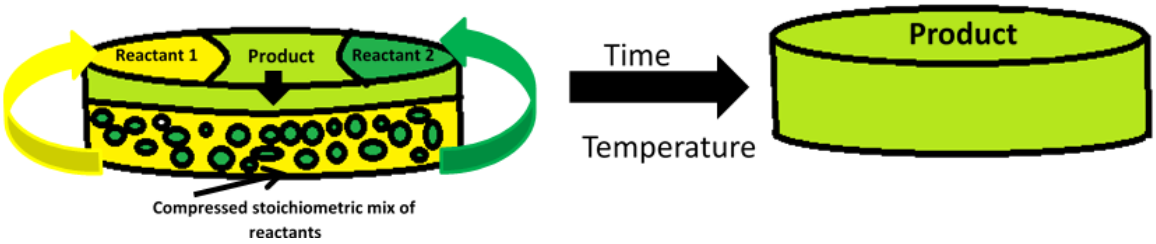

Figure 2.1 Solid state synthesis takes place when the rate of diffusion is enhanced using temperature and pressure. The reaction takes place when the reactants react on the surface and over time leads to the synthesis of the final product.

Stoichiometric amounts of oxides R_2O_3 (=La, Nd, Sm, Eu and Ga), GeO_2, Pr_6O_{11} and BeO (99.95% or higher purity) were mixed together and pressed in 1 cm diameter pellets under 10 kPa of pressure.

$$3A_2O_{3\,(s)} + 3Ga_2O_{3(s)} + 4GeO_{2(s)} + 2BeO_{(s)} \longrightarrow 2A_3Ga_3Ge_2BeO_{14\,(s)} \text{ (Reaction 2.1)}$$
(A=La, Nd, Sm, Eu)

$$Pr_6O_{11(s)} + 3Ga_2O_{3(s)} + 4GeO_{2(s)} + 2BeO_{(s)} \longrightarrow 2Pr_3Ga_3Ge_2BeO_{14\,(s)} + O_{2(g)} \text{ (Reaction 2.2)}$$

The obtained pellets were then heated in a platinum crucible at different temperatures (table 2.1).

Table 2.1 Synthesis temperatures for the newly synthesized langasites.

Compound	Synthesis temperature
$La_3Ga_3Ge_2BeO_{14}$	1300°C
$Pr_3Ga_3Ge_2BeO_{14}$	1250°C
$Nd_3Ga_3Ge_2BeO_{14}$	1300°C
$Sm_3Ga_3Ge_2BeO_{14}$	1290°C
$Eu_3Ga_3Ge_2BeO_{14}$	1300°C

The samples were heated at the above mentioned temperatures for 24-48 hours with intermittent grindings. It should be noted that the synthesis of these Be-langasites require working with BeO which must be handled with special precautions as Beryllium is listed as a Group 1 known human carcinogen by the international agency for research on cancer [64]. Special precautions were taken during the synthesis and handling of the final products. Use of lab coat, gloves, safety goggles and inhalation masks was made to avoid skin contact and inhalation. The grinding of the samples was carried out in a well ventilated fume hood. During and after synthesis, the samples were stored in MSDS labelled air tight containers in the desiccator. It is worth noticing that the mass of BeO used per reaction is small (about 2% (w/w)) for each reaction that yields 2 grams of final product thus very small quantities of BeO are dealt with at a time.

Although Mill *et al.* [19], [65] first reported the synthesis of members of this series, no x-ray refinements were presented for these compounds. This thesis reports the characterization of these compounds using x-ray diffraction, magnetization, magnetic susceptibility, heat capacity, MuSR and neutron scattering measurements.

2.2 Crystal Growth

The Travelling Floating Zone (TFZ) technique was used to grow crystals of the langasites. The process of crystal growth begins by compressing the powder in the form of cylindrical rods of 10 mm diameter using cylindrical balloons. The arrangement is then connected to a vacuum line to remove all air trapped within the sample. After this the sample is secured by tying two knots, making sure no air enters the assembly in the process. Using a hydrostatic press, a pressure of 30 kPa is applied for two minutes to obtain the rods. The obtained rods are then sintered for 12 hours at 1000 ° C in air before using them for crystal growths.

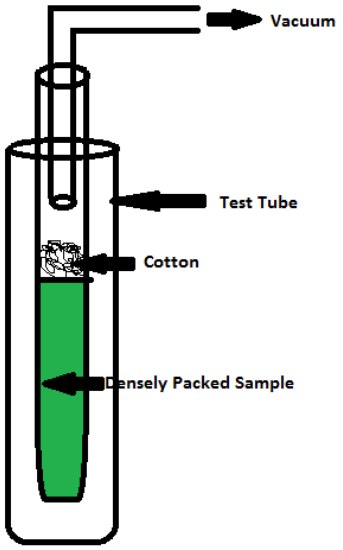

Figure 2.2 Process of packing powder to form rods for crystal growth

To prepare for crystal growth, one rod is attached to the seed rod holder and the other one is hung on the feed rod using a platinum wire. Halogen or xenon lamps are used to heat the sample to high temperatures. Once a high enough temperature is achieved, the crystal growth process starts with the melting of the tips of polycrystalline rods. Once the tips of both rods are melted they are brought together and joined to establish a liquid called the floating zone. After the successful creation of a stable zone, the rods are translated downwards at a certain speed and this is referred to as the speed of crystal growth. When the rods move out of the hot zone, the liquid cools and the material eventually crystallizes on the seed rod and thus a crystal is obtained. During growth, the rods also rotate in opposite directions

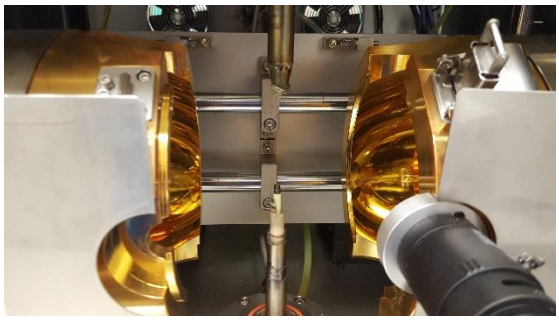

Figure 2.3 The inside of a Quantum Design image furnace showing a grown crystal.

at a certain rate to ensure homogenous mixing of the materials in the hot zone. Crystal growth was attempted on three members of the langasite family- $Pr_3Ga_3Ge_2BeO_{14}$, $Nd_3Ga_3Ge_2BeO_{14}$ and $Sm_3Ga_3Ge_2BeO_{14}$.

Table 2.2 Rod translation rate of the three langasite crystals.

	Rod Translation
$Pr_3Ga_3Ge_2BeO_{14}$	15 mm/hr
$Nd_3Ga_3Ge_2BeO_{14}$	20 mm/hr
$Sm_3Ga_3Ge_2BeO_{14}$	15 mm/hr

The growth environment is another factor that can control the quality of the crystal. Some compounds have a high vapour pressure. This can be a problem during the growth as the material will not crystallize and escape the system. Another challenge is the possibility of a phase transition. Some materials are sensitive to oxygen for example, and if the growth is done in air the end product will not be phase pure. This problem can be solved by controlling the environment of the growth. For the langasites, a one percent mixture of oxygen in argon was used for a successful growth.

A premelt is the process of running the crystal through the hot zone at a faster rate and then running it again at a much slower rate to enhance the quality of crystal. For incongruently melting crystals, a premelt is a great way to enhance the quality. All three langasite crystals were grown from a premelt.

Table 2.3 Premelt and growth rates for the langasite crystals.

	Premelt	**Growth rate**
$Pr_3Ga_3Ge_2BeO_{14}$	10 mm/hr	2 mm/hr
$Nd_3Ga_3Ge_2BeO_{14}$	10 mm/hr	1 mm/hr
$Sm_3Ga_3Ge_2BeO_{14}$	10 mm/hr	2 mm/hr

2.3 X-Ray Diffraction

Powder x- ray diffraction is an important tool in solid state chemistry for crystal structure identification. Diffraction data can provide details about the sample including particle size, homogeneity of particle size, lattice parameters and so on. For samples containing more than one phase, the different phases can be identified quantitatively [43].. For this study, room temperature powder X-ray data were collected on 30-40 mg of samples using the Huber Image Plate Guinier camera G670, $CuK_{\alpha 1}$ radiation (λ =1.5405981 Å) for a range of $10^{o} \leq \Theta \leq 100^{o}$ for all samples.

2.3.1 Huber G 670 Guinier Camera

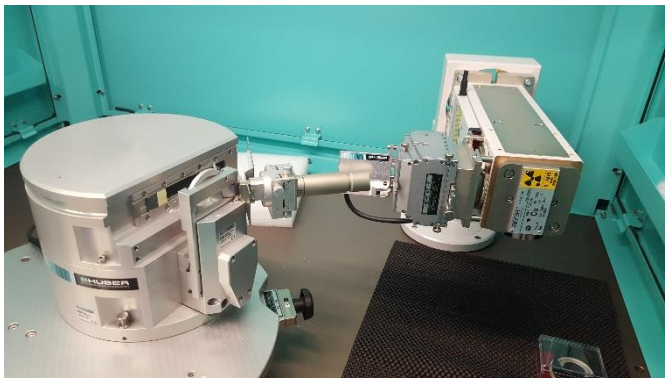

Figure 2.5 Working of a Huber Guinier G670 diffractometer with different parts labelled.

The Huber G670 has a flat plate Guinier (transmission) geometry and a linear imaging plate detector. The two-theta range covered by the diffractometer is between 0 and 100 degrees. A slurry of powdered sample mixed with methanol is applied to the mylar film on the sample

holder and is left to dry. The detector is made of a polyester coated with a homogenous powder consisting photo-stimulable phosphor. The phosphor consists of barium fluoro-bromide with trace amounts of europium [66]. The sample holder sits between the x-ray beam and detector. A Ge (111) bent crystal monochromator was used here to filter out interfering components of x-rays like K_β and $K_{\alpha 2}$ and increases the resolution of the resultant diffraction pattern. The anode, which is the source of x-rays, used here is Cu. The cathode used in this case is tungsten. The image plate consists of an integrated circuit which stores the output of the scan. The plate containing the output is scanned by a laser, and the output is displayed as sharp Bragg peaks and stored as data files. One advantage of Guinier transmission geometry is that high quality data can be obtained with very little exposure time. Once the scan is complete and the data is properly stored, the imaging plate containing the data is erased using a halogen lamp before the next run [66], [67].

2.4 Magnetism

The magnetic properties of the langasites were explored using the Quantum Design Physical Property Measurement System (PPMS).

Both the field cooled and zero field cooled d.c. susceptibility was measured as a function of temperature using the Vibrating Sample Magnetometer (VSM) on powder samples ranging in mass from 10-30 mg. Measured quantities of samples were loaded in a polypropylene powder sample holder and attached to the brass trough.

Figure 2.6 A non-magnetic brass trough with polypropylene sample holder. The magnetic response is generated only from the sample.

Figure 2.7 A sample holder rod with brass trough containing the polypropylene sample holder on one end.

The brass trough is then screwed into a sample holder rod and the sample is installed in the PPMS. An advantage of using the polypropylene sample holder with a brass trough is that there is no need for a background subtraction as both the materials are low background moment holders and are non-magnetic.

The magnetization measurements are also carried out using the VSM option of the PPMS. The measurement is different from DC susceptibility in terms of the parameters that are varied over time. Magnetization measurements are carried out at a fixed temperature but varying the applied magnetic field. The moment is recorded as a function of the field going from 0 to 9 T and from 9 to 0 T. Magnetization measurements were carried out at four different temperatures of 0.500 K, 2 K, 5 K and 30 K up to a field of 9T.

2.4.1 Vibrating Sample Magnetometer (VSM)

The sample rod is inserted into the measurement chamber to take measurements. The linear motor vibrates the sample in magnetic field. The measurement is taken by detecting the voltage induced by change in magnetic flux of the sample. The sample is centered once it is installed to find the exact distance between the sample and the coil set. [68]

Figure 2. 8 Vibrating Sample Magnetometer by Quantum Design.

2.4.2 Heat Capacity

The heat capacity measurements were performed on the langasites using the helium-3 insert of the PPMS. The heat capacity is measured using the normal heat capacity option down to 1.8K. When the temperature goes below that, the helium-3 option is activated.

The working principle of the instrument is to monitor the heat supplied to the sample being measured and the heat removed from it while monitoring the change in temperature of the sample. The heat capacity software fits the behaviour of the temperature of the sample platform so that it takes into account the thermal relaxation of the platform and the sample. The measurements are performed by compressing samples in forms of small pellets (1-2 mm dia) and adhering them to the measurement puck using grease. For measurement below 300 K, Apiezon N grease is used as it is less viscous and hardens as the temperature is lowered and thus enhances the contact between the sample and platform. The second type is the Apiezon H grease, which is used for measurements above 300 K. This grease is viscous and does not melt or vaporize at higher temperatures. To ensure that there is no loss of heat during the exchange process, heat capacity measurements are done in a high-vacuum system. A charcoal holder is used to decrease the pressure at the bottom of the puck as the temperatures approaches below 10 K. A platform heater and platform thermometer are attached to the bottom side of the sample platform to track all temperature changes.

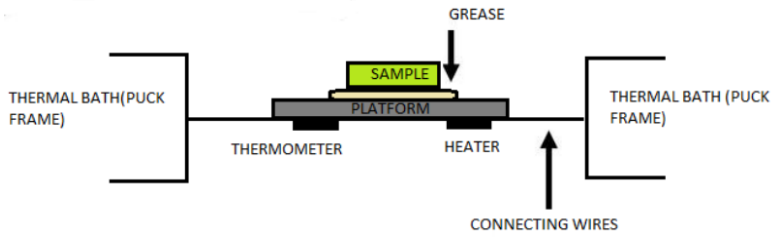

Figure 2.9 The sample is adhered to the puck using grease. The heat capacity of grease is subtracted from the total to find the heat capacity of the sample (adapted from [91]).

2.5 Muon Spin Resonance/Relaxation/Rotation (μSR)

Muon spin resonance studies were carried out on $Nd_3Ga_3Ge_2BeO_{14}$ at TRIUMF (Vancouver). Dilution refrigerator was used to perform measurements in at a low temperature of 0.030 K and the measurements were carried out for a temperature range of 0.030 K to 6 K. A magnet was also used to understand the behaviour of the material under applied field (both transverse and longitudinal).

2.5.1 Formation of Muons

The process starts with the high energy neutrons or protons (600-800 MeV) striking a target made of an element with low Z. This results in the emission of pions [56], [58], [69].

$$p + p \longrightarrow \Pi^+ + p + n \quad \text{or} \quad p + n \longrightarrow \Pi^+ + p + n \qquad \text{(Reaction 3)}$$

where p is a proton, n is a neutron and Π^+ is a pion.

The pion particles have a half-life of 26 nanoseconds and are very unstable. As soon as they are formed they decay further and result in the release of muons and neutrinos as additional products

$$\Pi^+ \longrightarrow \mu^+ + \nu_\mu \quad \text{or} \quad \Pi^- \longrightarrow \mu^- + -\nu_\mu \qquad \text{(Reaction 4)}$$

Where μ are muon particles and ν_μ are muon neutrinos/anti-neutrinos.

Thus the muons are formed. As mentioned previously, muons are highly unstable and therefore they further decay into even smaller particles.

$$\mu^+ \longrightarrow e^+ + \nu_e + -\nu_\mu \quad \text{or} \quad \mu^- \longrightarrow e^- + -\nu_e + \nu_\mu \qquad \text{(Reaction 5)}$$

where ν_e are electron neutrinos/anti-neutrinos.

Once the muons are formed, they are directed to the sample. When directing muons to the sample, special effort is made to get rid of any additional particles formed as a by-product of the decay process. This results in a reduction of false counts on the detector and also protects the sample from additional radiations [56]–[58], [69], [70].

In order to perform measurements, the muons are fired on the sample of interest. Polarized muons that have just enough energy to stop within the sample and not pass it are planted in the samples.

Due to momentum conservation, a pion decaying at rest will result in muons and neutrinos with opposite momentum with respect to that of the pion. This means that the muon and muon neutrino will have opposite spin and since they form the muon beam, the beam will be polarized. The spin polarized muons, after getting planted in the sample, are monitored for the polarization of the muon as a function of time. This provides information regarding the local spin environment at each site where the muon is planted [57].

2.6 Neutron Scattering

2.6.1 Inelastic Neutron Scattering on $A_3Ga_3Ge_2BeO_{14}$ (A= Pr, Nd)

The Disc Chopper Spectrometer (DCS) is a time of flight spectrometer where the pulsed and monochromated neutrons, produced from multiple choppers are used for measurements. The neutrons get scattered from the sample and get detected by the detector [71]. The time of flight analysis of the scattering is used to determine the energy and the momentum transfer.

DCS is a direct geometry instrument. The beam filters are placed in the beam to get rid of high energy neutrons and gamma radiation using a crystal filter made of graphite [72].

After getting filtered, the neutron beam travels to seven disk choppers in four housings. The housings contain the choppers that monochromate and pulse the incoming beam. Depending on the type of measurement, the chopper speed can be set anywhere between 1200 and 20,000 revolutions per minute [72]. After the choppers, the beam enters the sample chamber. The sample chamber contains a radial collimator which minimizes scattering from the sample environment.

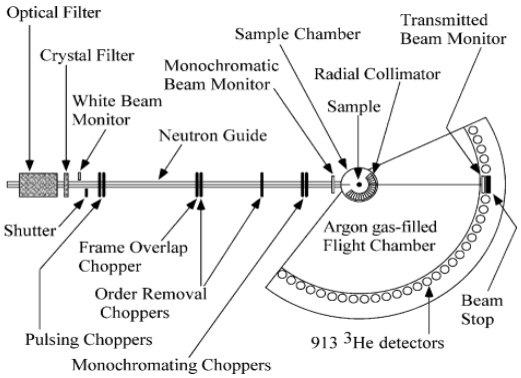

Figure 2.10 Working of Disk Chopper Spectrometer (DCS) at National Institute of Standards and Technology (NIST) (Used with permission) [72].

The sample environment is usually filled with a weakly scattering gas like argon. After getting scattered from the sample, the beam travels towards the detector. A total of 913 detectors are present which are filled with He-3. The detectors are separated in three banks for different scattering angle ranges [72].

The DCS is a cold neutron source which was used to perform elastic and inelastic neutron scattering measurements on $A_3Ga_3Ge_2BeO_{14}$ (A= Pr, Nd).

About 10 grams of powdered sample of each was put in a copper can in an Ar environment and was packed tightly to avoid displacement of the sample during measurement. The measurements

were performed for a fixed wavelength of 4.8 Å for 0, 6 and 9 T fields and a temperature range of 0.070 K to 50 K.

2.6.2 Diffuse Scattering Measurements on $Nd_3Ga_3Ge_2BeO_{14}$

The diffuse scattering spectrometer is a polarized neutron beam spectrometer which is used to understand the magnetism of materials, mainly short range ordering and defects in frustrated systems. It has also been used to study non-collinear ferromagnetism, hydrogen diffusion in metals and single and collective particle excitations [111].

D7 is a cold neutron time of flight diffractometer with multiple detectors. The nuclear, magnetic and nuclear-spin scattering contributions can be can be separated over Q. This makes it ideal for the study of magnetic materials with disorder [73].

The D7 can be operated in three settings under the diffraction mode.

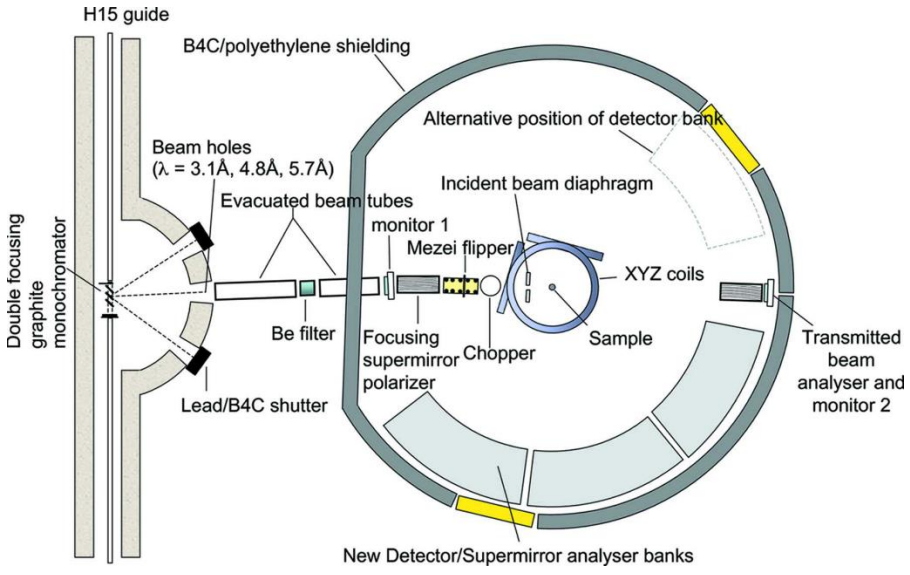

Figure 2.11 Working of Diffuse Scattering Spectrometer (D7) at Institut Laue–Langevin (ILL)(Reproduced with permission of the International Union of Crystallography [75]).

Diffraction can be performed on both powders and single crystals. The polarization direction at the sample can be adjusted in three ways. The first is the uniaxial polarization analysis where the direction of polarization is perpendicular to scattering plane. In this case, the spin-flip and non-spin flip scattering is recorded. This setting is useful when separating coherent and incoherent scattering contributions in nonmagnetic samples [74], [75]. The second setting is the XYZ polarization, where the polarization directions change. They change between the three orthogonal directions and the spin-flip and non-spin-flip scattering is measured. This is also called the 6 point method. The last setting is the 10 point measurement. Here instead of three, there are five directions of measurements. The five directions in which measurements are made are 1. Normal to the scattering plane, 2. Two orthogonal directions in scattering planes, 3. Two orthogonal directions at an angle of 45 deg to the scattering planes. The instrument measures spin flip and non-spin flip scattering at each of these five positions [74], [75]. From this, the different neutron cross sections are extracted. Diffuse scattering measurements were conducted for the $Nd_3Ga_3Ge_2BeO_{14}$ sample at ILL for 4.8Å wavelength.

The data was collected at 0.035 K, 1.2 K, 10K and 40 K. The 40 K data was used to subtract the background contributions. The measurement was performed on powdered sample.

Chapter 3

Synthesis and Structural Properties of $A_3Ga_3Ge_2BeO_{14}$ (A= La, Pr, Nd, Sm and Eu)

3.1 Synthesis

Successful synthesis was carried out for $A_3Ga_3Ge_2BeO_{14}$ (A= La, Pr, Nd, Sm and Eu) using the solid state synthesis technique described in chapter 2. By x-ray diffraction it was confirmed that the langasite phase is stable for these lanthanide substitutions. Langasite compounds with different substitutions have been synthesized before [17], [24], [76]. ($Pr_3Ga_5SiO_{14}$) PGS and ($Nd_3Ga_5SiO_{14}$) NGS are two well characterized langasites that have been synthesized and characterized extensively and have shown evidence of spin liquid phenomena [21], [77], [78]. After getting successful results from these compounds, Zhou *et al.* expanded the synthesis to the other members of the rare-earth series [79]. The next substitution for the langasite series would have been Sm but the synthesis of $Sm_3Ga_5SiO_{14}$ was restricted by the formation of a competing garnet phase $Sm_3Ga_5O_{12}$.

$$Sm_3Ga_5SiO_{14} \longrightarrow Sm_3Ga_5O_{12} + SiO_2 \quad \text{(Reaction 3.1)}$$

After the analysis of the ionic radii, it was realized that the stability field of the langasite phase collapses as one moves from Pr (1.126 Å) and Nd (1.109 Å) to Sm (1.079 Å) because of the decrease in ionic radii of Sm^{3+}, a result of lanthanide contraction in the rare earth series. The smaller size of Sm^{3+} destablizes the langasite struture and favours a more symmetric garnet structure.

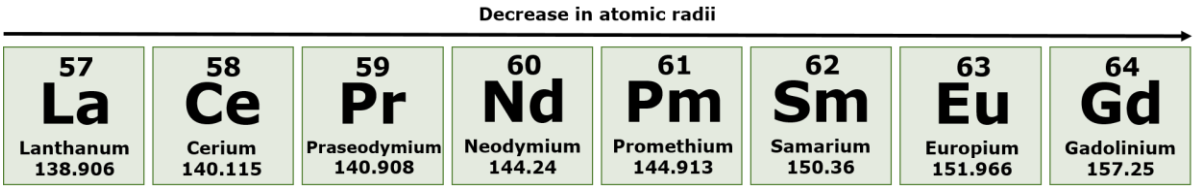

Figure 3.1 Decrease in atomic radii as one moves from left to right in the rare-earth series due to the lanthanide contraction.

More attempts were made to synthesize a Sm-langasite by substituting some of the Ga sites with Al. Some previously reported Sm langasites include $Sm_3Ga_{2.63}Al_{2.37}SiO_{14}$ [24] and $Sm_3Ga_2Al_3SiO_{14}$ [25]; both of these Sm-langasites could be prepared with the presence of some garnet impurity phase.

In order to further understand the magnetic properties of langasites, synthesis and characterization of new members was necessary.

One approach to stabilize the smaller rare earth ions on a langasite structure was to decrease the overall size of the lattice to accommodate smaller cations. This thesis reports on five new langasites that were synthesized by substituting some of the gallium sites with germanium and the silicon site with beryllium. The chemical formula of the new langasites is $A_3Ga_3Ge_2BeO_{14}$ where the A site was successfully substituted with La, Pr, Nd, Sm and Eu.

Table 3.1 Summary of synthesis of langasite members with different rare-earths on the A site

New langasites with different rare-earths on the A site	
$La_3Ga_3Ge_2BeO_{14}$	Synthesized
$Ce_3Ga_3Ge_2BeO_{14}$	Not attempted
$Pr_3Ga_3Ge_2BeO_{14}$	Synthesized
$Nd_3Ga_3Ge_2BeO_{14}$	Synthesized

$Pm_3Ga_3Ge_2BeO_{14}$	Not attempted
$Sm_3Ga_3Ge_2BeO_{14}$	Synthesized
$Eu_3Ga_3Ge_2BeO_{14}$	Synthesized
$Gd_3Ga_3Ge_2BeO_{14}$	Attempted but unsuccessful
$Gd_3Al_3Ge_2BeO_{14}$	Attempted but unsuccessful

Synthesis of the Ce member was not attempted as, unlike the other rare-earths in the series, Ce favours a 4+ oxidation state as opposed to 3+. Also, Ce^{4+} is non-magnetic and Ce^{3+} cannot be stabilized for the langasite structure. Another member that was skipped in the series was Pm as all of its isotopes exist in radioactive form. After successfully synthesizing Eu, the next step was to substitute Gd on the A site. This substitution failed, however, as the structure stability collapsed once again and the final product had a 50% garnet phase and a 30% langasite phase along with unreacted reactants as impurities. Following the same logic as before, Ga was substituted for Al and synthesis of $Gd_3Al_3Ge_2BeO_{14}$ was attempted but the obtained product showed a mixture of a 60% langasite phase along with a 40% garnet phase impurity. Going from Eu^{3+} (VIII) to Gd^{3+} (VIII), there is a decrease in ionic radii from 1.066 Å for Eu to 1.053 Å for Gd [80], which leads to the formation of a competing garnet phase along with the langasite phase.

3.2 The Kagomé Lattice and Coordination of the Different Sites

The langasites with A-site cations La, Pr, Nd, Sm and Eu in $A_3Ga_3Ge_2BeO_{14}$ stoichiometry are magnetic in nature because of the presence of unpaired 4f electrons. The langasites have a trigonal crystal structure where the magnetic ions occupy the corners of the triangular network forming a distorted 2-D Kagomé lattice. The Kagomé planes are stacked along the c-axis. The langsites form a distorted Kagomé system instead of an ideal system. A distorted Kagomé is

formed when only the nearest neighbour interactions are considered for the magnetic ions and the bond angles are not ideal [81]. In the new Kagomé langasites, the magnetic ion site is 8-fold coordinated and forms a distorted square antiprism. The site is occupied by Gallium and is in octahedral coordination. The site shared between Germanium and Gallium is in tetrahedral coordination and the site shared between Beryllium and Germanium is also in tetrahedral coordination.

Table 3.2 Positions and coordinations of ions on different sites in the new langasites.

Site	Position	Coordination
Magnetic ion	(0.42,0,0)	8- fold coordinated distorted square antiprism
Ga	(0,0,0)	Octahedral
Ga/Ge	(0.76, 0, ½)	Tetrahedral
Ge/Be	(1/3, 2/3, 0.53)	Tetrahedral

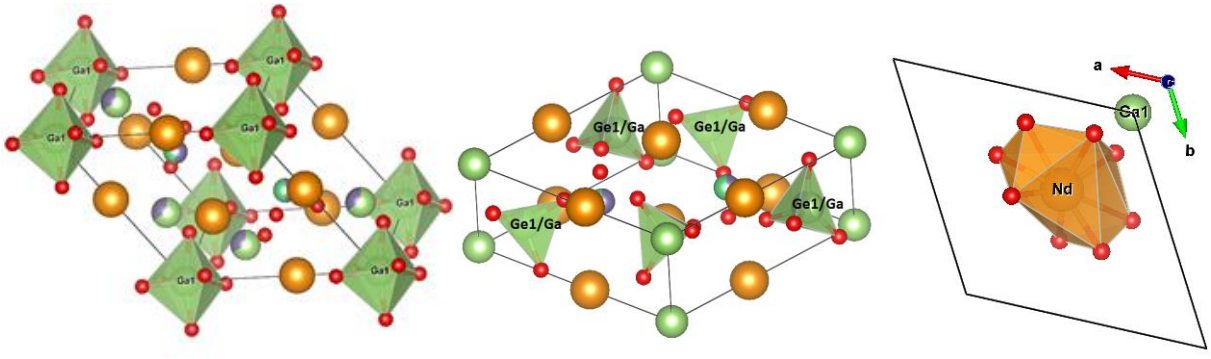

Figure 3.0.2 Octahedral (left), tetrahedral (middle) and 8-fold coordination (right) of the ions on different sites in the Be-langasites.

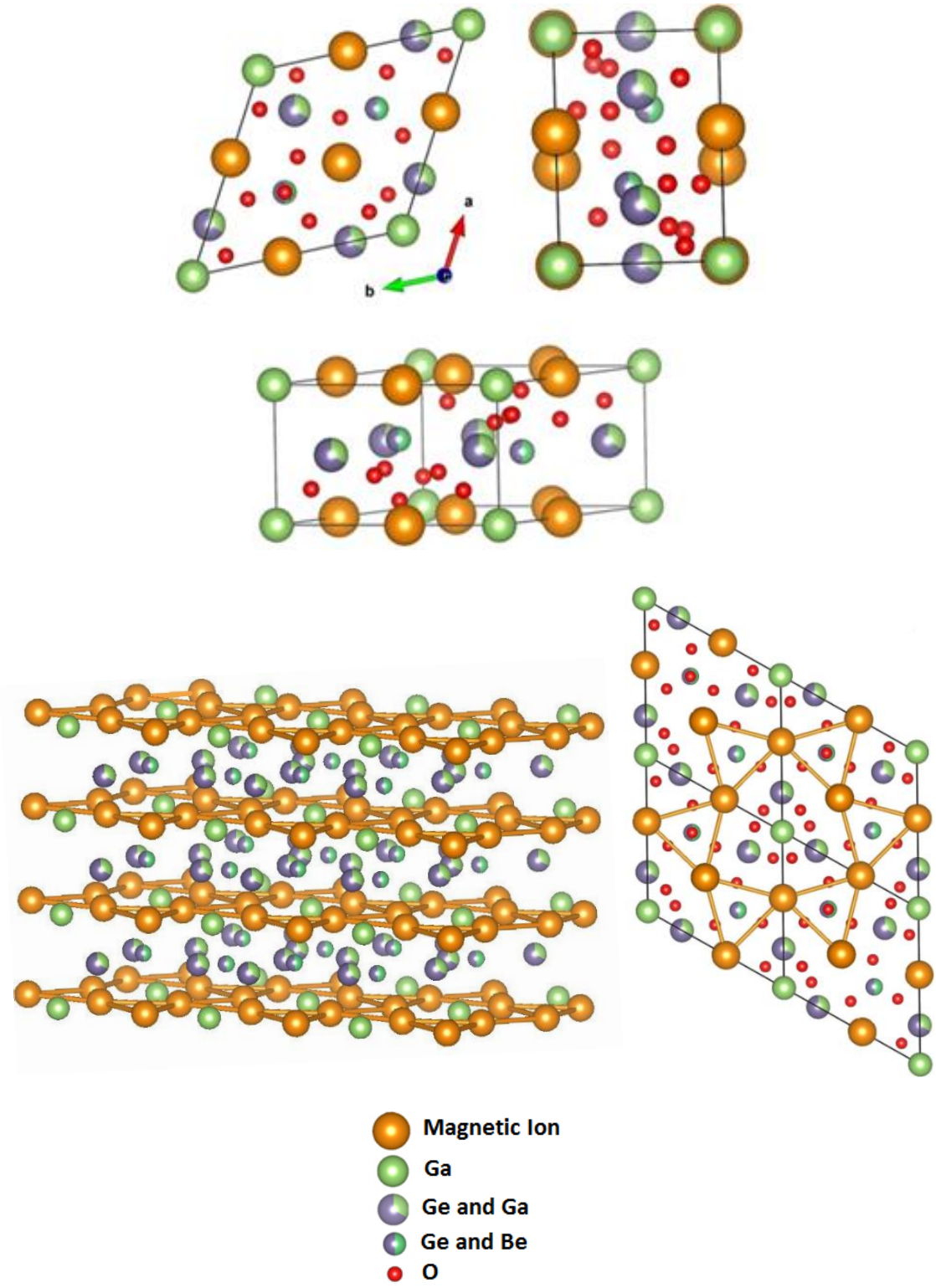

Figure 3.3 (top) Unit cell of the Be-langasites viewed along different planes. (bottom, left) Well separated planes of corner sharing triangles forming a Kagomé network. (bottom, right) Kagomé net formed by magnetic ions in Be-langasites [16]**.**

3.3 X-Ray Diffraction and Rietveld Refinement

The experimental powder X-ray diffractograms and Rietveld refinements of the five new langasites (four with magnetic ions and a lattice standard) a) $La_3Ga_3Ge_2BeO_{14}$ b) $Pr_3Ga_3Ge_2BeO_{14}$ c) $Nd_3Ga_3Ge_2BeO_{14}$ and d) $Sm_3Ga_3Ge_2BeO_{14}$ e) $Eu_3Ga_3Ge_2BeO_{14}$ are shown in figure 3.4. [16] By looking at the difference between the experimental and theoretical pattern, it can be seen that the experimental data is in complete agreement with the theoretically calculated pattern.

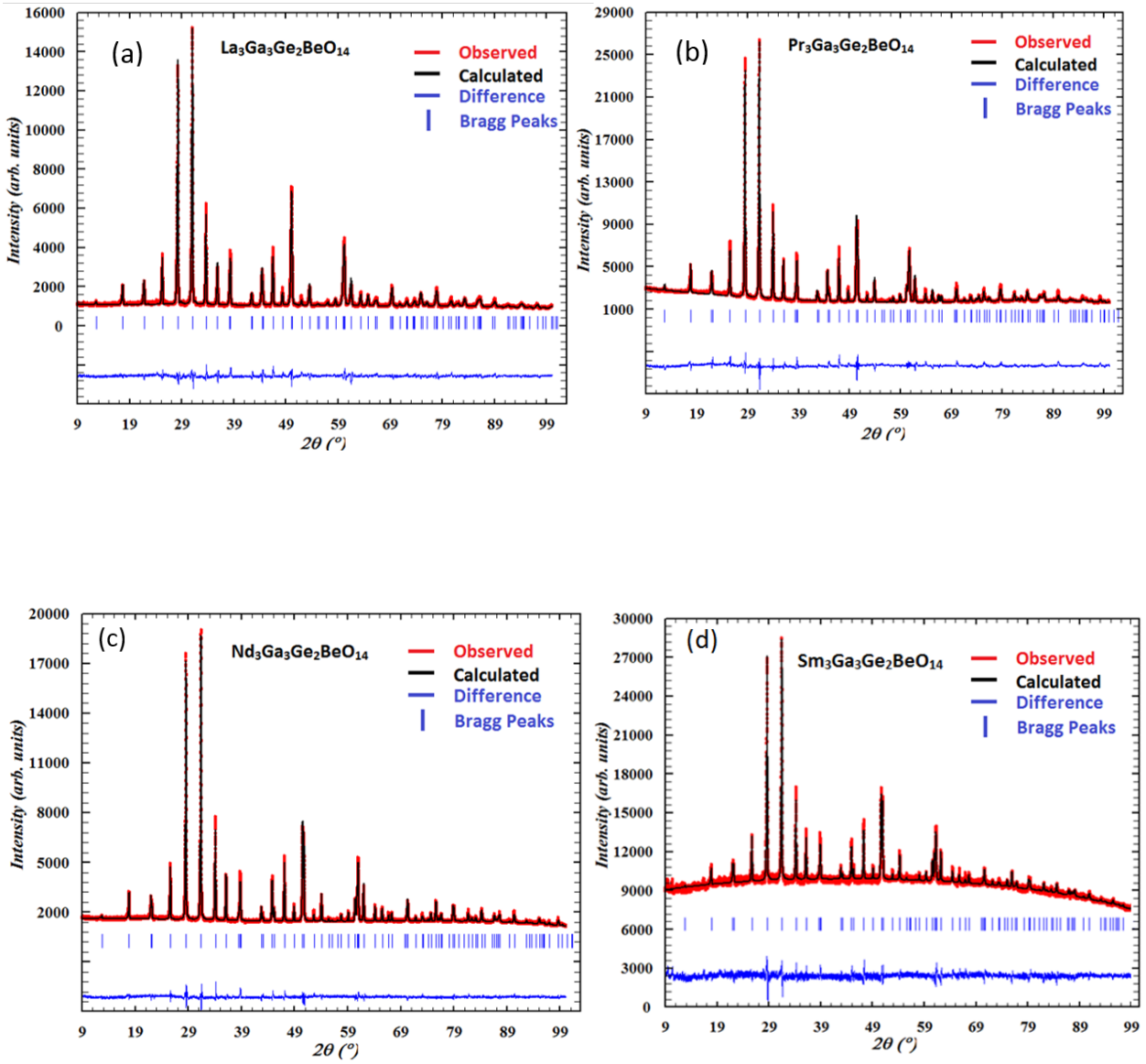

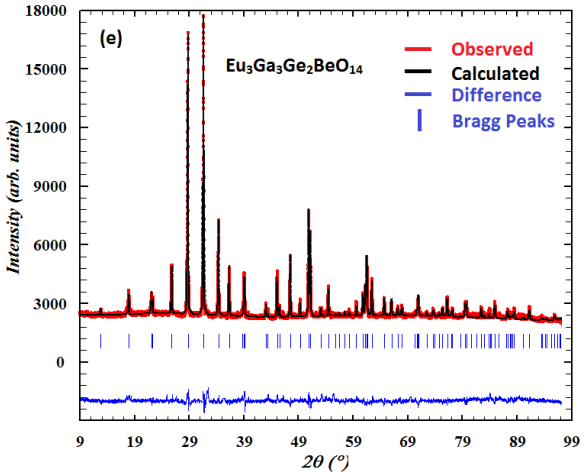

Figure 3.4 Rietveld refinement patterns of the powder samples of (a) $La_3Ga_3Ge_2BeO_{14}$ (b) $Pr_3Ga_3Ge_2BeO_{14}$(c) $Nd_3Ga_3Ge_2BeO_{14}$ (d) $Sm_3Ga_3Ge_2BeO_{14}$ and (e) $Eu_3Ga_3Ge_2BeO_{14}$. (Red symbols- observed data, black symbols- calculated pattern, blue symbols- difference, blue tick marks – Bragg positions) [16].

The absence of any competing phase or unreacted starting products in all five patterns suggests that the langasite phase is more stable thermodynamically. The $Sm_3Ga_3Ge_2BeO_{14}$ diffraction pattern (figure 3.4 (d)) has a higher background as compared to the other langasites. This was a result of x-ray absorption by the Sm langasite. It is a feature of the instrument and has been observed in all other Sm containing compounds scanned using the Guinier G670 camera in the PRIME lab.

The lattice parameters and atomic positions for the langasites were determined using Rietveld structural refinements performed on the powder diffraction patterns. All five diffraction patterns were successfully indexed by a trigonal lattice with the space group P321. The crystallographic and lattice parameters are listed in Tables 3.3 and Table 3.4 respectively. The low R_P, R_{wp} and χ^2 values (Table 3.4) indicate a good match between the experimental and the calculated model. A slight decrease in lattice parameters and volume of the unit cells can be seen across the series going from $La_3Ga_3Ge_2BeO_{14}$ to $Eu_3Ga_3Ge_2BeO_{14}$. (Table 3.4) This is expected because of the decrease in ionic radii as one moves from the left to the right due to the lanthanide contraction in the rare earth series.

Table 3.3 Crystallographic parameters obtained for $La_3Ga_3Ge_2BeO_{14}$ at room temperature using Cu $K\alpha_1$ x-ray radiations (λ=1.54 Å).

	A	**Ga1**	**Ga2**	**Ge1**	**Be**	**Ge2**	**O1**	**O2**	**O3**
Wyckoff Positions	3*e*	1*a*	3*f*	3*f*	2*d*	2*d*	2*d*	6*g*	6*g*
x Coordinate	0.5852 (0.0006)	0	0.232 (0.001)	0.232 (0.001)	0.33333	0.3333	0.6667	0.419 (0.008)	0.232 (0.005)
y Coordinate	0	0	0	0	0.6667	0.6667	0.3333	0.115 (0.007)	0.143 (0.005)
z Coordinate	0	0	0.50000	0.50000	0.481 (0.005)	0.481 (0.005)	0.24 (0.02)	0.355 (0.007)	0.239 (0.005)
Occupancies	0.50000	0.16667	0.16667	0.33333	0.16667	0.16667	0.33333	1.00000	1.00000

Table 3.4 Lattice Parameters obtained for the synthesized langasites with space group P321 ($\alpha=\beta=90^o$, $\gamma=120^o$) [16].

	a (±0.002) Å	**c (±0.002) Å**	**Volume (±0.25) (Å^3)**	**R_p (%)**	**R_{wp} (%)**	**χ^2**
$La_3Ga_3Ge_2BeO_{14}$	8.129	5.008	286.60	4.3	4.99	1.46
$Pr_3Ga_3Ge_2BeO_{14}$	8.058	5.049	283.92	3.38	3.87	1.63
$Nd_3Ga_3Ge_2BeO_{14}$	8.026	4.957	276.54	2.95	3.28	1.66
$Sm_3Ga_3Ge_2BeO_{14}$	7.990	4.956	273.69	5.24	5.59	1.56
$Eu_3Ga_3Ge_2BeO_{14}$	7.953	4.948	272.03	2.88	4.30	1.95

3.4 Bond Valence Analysis

Bond valence analysis was performed on the structural data obtained from x-ray diffraction. The analysis was carried out for $La_3Ga_3Ge_2BeO_{14}$. The obtained bond valence sums for different ions are shown in table 3.5. In future work, comparison will be made between the bond valence sums (obtained from x-ray diffraction and neutron scattering combined data refinement) of the different members of the family.

Table 3.5 Bond valence analysis of $La_3Ga_3Ge_2BeO_{14}$ performed using EdPCR (FullProf) [82] . The table shows bond valence sums, coordination and average oxygen bond distance for different ions in the structure.

Atom	Bond Valence	Coordination	Obtained Average Oxygen Bond Distance (Å)
La^{3+}	3.01	8	2.534
$Ga1^{3+}$	2.99	6	1.986
$Ga2^{3+}$	3.05	4	1.6304
$Ge1^{4+}$	4.5	6	1.63
Be^{2+}	1.98	4	1.1245
$Ge2^{4+}$	3.67	4	1.7480

$O1^{2-}$	**2.28**		
$O2^{2-}$	**2.04**		
$O3^{2-}$	**1.74**		

From the table above, a comparison can be made between the obtained bond valence sums and the expected oxidation states. The results are in good agreement for La however for other ions they vary from the expected numbers. There are many reasons that can lead to this

- The obtained results are not very reliable when the analysis is done using x-ray diffraction on Ga and Ge. The ions cannot be easily distinguished by conventional x-ray diffractometers because of their similar electron environment. The lab x-ray beam, which interacts with the electron cloud of an atom, cannot distinguish between the two atoms effectively.
- In the Be-langasites the participating atoms have very different sizes. The presence of heavier atoms like the rare earths (La, Pr, Nd, Eu etc.) in the system makes it very difficult for the atoms with smaller electron cloud like O and Be to be detected.
- The bond valence sum was off by 12 (3) % for mixed sites (Ga/Ge and Ge/Be) as random mixing of ions occurs which are expected to have different bond lengths with O.

Bond valence analysis provided some information about the oxidation states of the ions involved. More accurate results can be obtained by a combined x-ray and elastic neutron scattering data refinements.

3.5 Crystal Growth

Single crystal growth using the optical floating zone image furnace was attempted for $Nd_3Ga_3Ge_2BeO_{14}$, $Pr_3Ga_3Ge_2BeO_{14}$ and $Sm_3Ga_3Ge_2BeO_{14}$. The crystals were about 3 cm in length with very little oxygen defects as determined by x-ray diffraction and final colours of the crystal. The colours of the obtained crystals are what is expected for the magnetic ions i.e. purple for Nd^{3+}, green for Pr^{3+} and yellow for Sm^{3+}.

Figure 3.5 Single crystals of Be-langasites grown using floating zone image technique (left) $Nd_3Ga_3Ge_2BeO_{14}$, (middle) $Pr_3Ga_3Ge_2BeO_{14}$ and (right) $Sm_3Ga_3Ge_2BeO_{14}$.

X-ray diffraction and Rietveld refinement were done to confirm the phase purity of the grown crystal. During the FZ technique high amounts of energy are supplied to the sample and sometimes the heat of the hot zone during the growth is enough to provide thermal energy to ions which might lead to transition to a metastable state thus leading to a phase transition during growth. X-ray diffraction was performed on crushed crystals. It was confirmed that after crystal growth all compounds retained the desired langasite phase. The obtained lattice parameters were in agreement with the powder x-ray diffraction data. Upon further investigation of these grown crystals it was realized that they contain multiple tiny single crystals within the large crystal.

Chapter 4

Magnetism of $Nd_3Ga_3Ge_2BeO_{14}$

4.1 D.C. Susceptibility

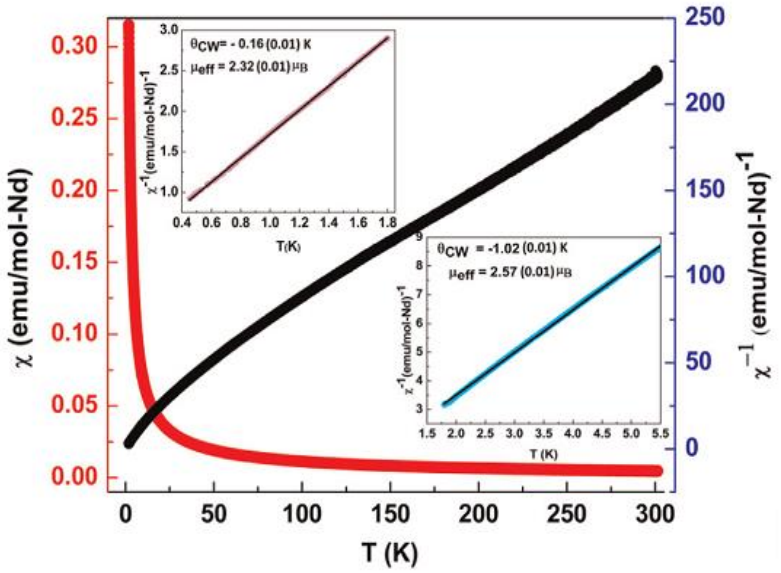

Figure 4.1 : Magnetic susceptibility and inverse susceptibility as a function of temperature (inset: Curie–Weiss fits) for $NdGa_3Ge_2BeO_{14}$ [16].

Figure 4.1 shows the d.c. susceptibility (red) and inverse d.c. susceptibility (black) as a function of temperature. There is a complete overlap between field cooled and zero field cooled susceptibility which indicates an absence of glassiness or ferromagnetism in the material. Curie-Weiss fits at high temperature (above 50 K) were attempted for $Nd_3Ga_3Ge_2BeO_{14}$ and the θ_{CW} and μ_{eff} obtained were -37.78 (0.03) K and 3.54 (0.05) μ_B respectively. The magnitude of θ_{CW} is very high which indicates the presence of crystal field terms. In order to avoid a contamination from crystal field population, the fits were done in different low temperature regions. The Curie-Weiss temperatures obtained for 1.8 K to 8 K fits was -1.02 (0.01) K and the effective magnetic moment was calculated as 2.57 (0.01) μ_B. For fits between 0.500 K and 1.8 K, the Curie-Weiss temperatures and effective moments obtained were -0.16 (0.01) K and 2.32 (0.01) μ_B. A negative

θ_{CW} confirms the antiferromagnetic nature of interactions. The calculated effective moment is smaller than the effective moments of Nd^{3+} (3.62 μ_B) [54]. The fits confirm the presence of antiferromagnetic interactions for $NdGa_3Ge_2BeO_{14}$. A smaller than expected effective moment is indicative of screening effects typical of frustrated magnets.

4.2 Magnetization

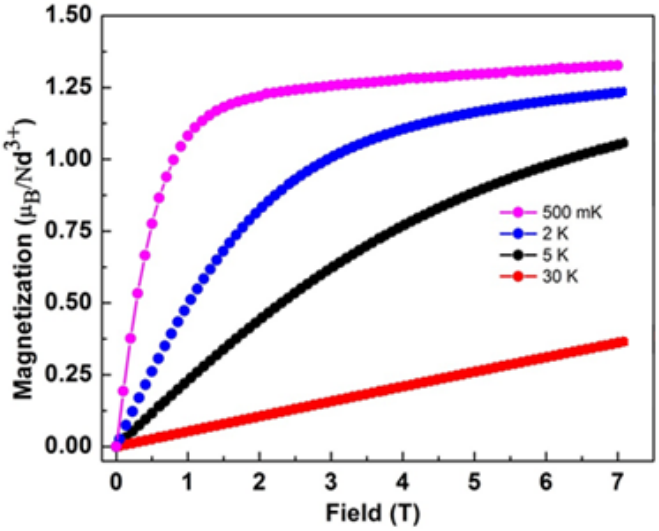

Figure 4.2 Magnetization curves for $Nd_3Ga_3Ge_2BeO_{14}$ at 0.500 K , 2 K, 5 K and 30 K in up to 7 T field [16].

The magnetization as a function of field from 0 to 7 T for $Nd_3Ga_3Ge_2BeO_{14}$ is shown in figure 4.2. It can be seen that the magnetization starts to saturate at 2K and when the temperature is further reduced to 0.500 K, magnetic moment appears to reach saturation. A Brillouin function fit (4.1) was performed on the 0.500 K data to further understand this behaviour.

$$B_J(x) = \frac{2J+1}{2J}\coth\left(\frac{2J+1}{2J}x\right) - \frac{1}{2J}\coth\left(\frac{x}{2J}\right) \tag{4.1}$$

$$\text{where} \qquad x = \frac{g_J \mu_B J B}{k_B T}$$

The magnetization increases with field for small fields but as the field is increased it reaches a saturation magnetization given by $N\mu_H = Ng\mu_B J$ where N is the number of atoms per unit volume and μ_H is the maximum moment of each atom in direction of H [52]. This corresponds to the maximum possible alignment of moments with the external field. The saturated moment for the Nd-langasite at 0.500 K was compared to a nonlinear least squares Brillouin function for J=9/2

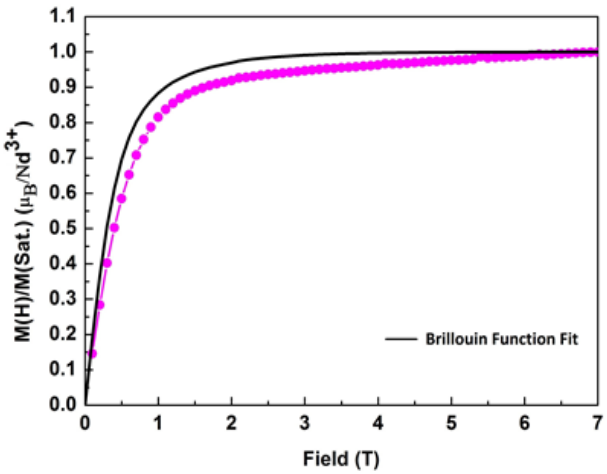

Figure 4.3 Brillouin function fit for $Nd_3Ga_3Ge_2BeO_{14}$ for 0.500 K data [16].

For Nd^{3+} J=9/2 but this state splits into five Kramers doublets in the crystal field of the magnetic ion [83]. Since Nd^{3+} is a Kramers ion, a doublet ground state was assumed with J_{eff}= ½. From figure 4.3 it can be seen that the fit diverges from the obtained data set at T= 0.500 K. This indicates that even though a complete saturation of magnetic moment was observed, the system does not exhibit paramagnetism and there are magnetic correlations persistent even at a low temperature of 0.500 K.

4.3 Heat Capacity

For $Nd_3Ga_3Ge_2BeO_{14}$, the heat capacity (C) as a function of temperature (T) and C/T vs T for 0 and 9 T fields along with the lattice standard is shown in figure 4.4

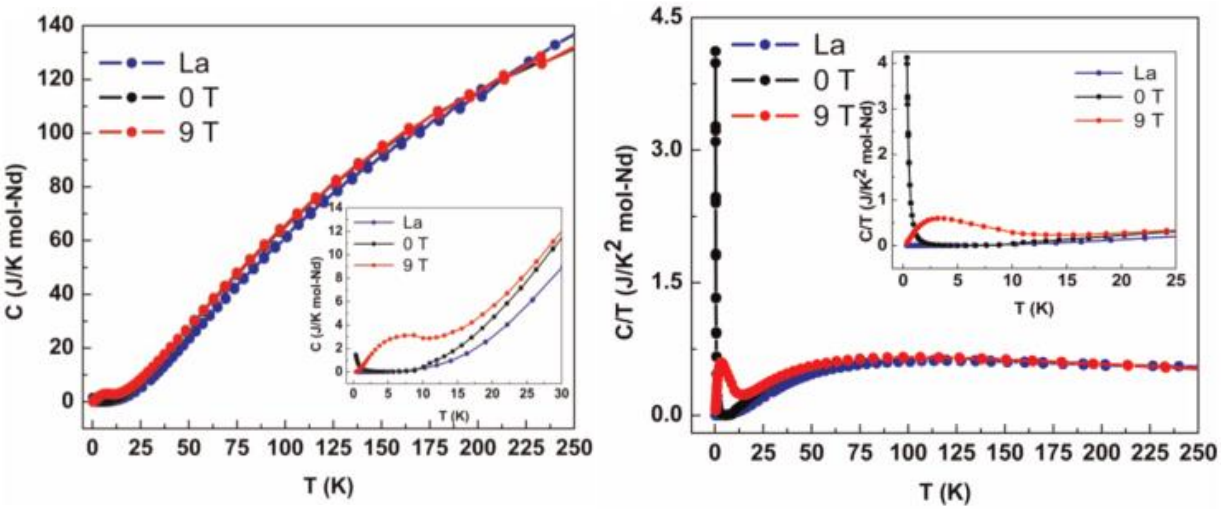

Figure 4.4 Heat capacity as a function of temperature at 0 T and 9 T and lattice standard for $Nd_3Ga_3Ge_2BeO_{14}$ (left) C/T vs. T data (right) [16].

From the plots (figure 4.4 (right)) it can be seen that for 0 T (black data set), below 3 K the heat capacity starts to increase with decreasing temperatures. This peak further shifts to higher temperatures and becomes broad as the field is increased to 9 T (red data set). This was assumed to be because of the characteristic splitting of the ground state doublet in the Nd-langasites (Nd^{3+} in the state $^4I_{9/2}$) in an applied magnetic field which leads to a sharp increase in the heat capacity at low temperatures also known as the Schottky anomaly. The Schottky fit to the heat capacity data after the lattice subtraction is shown in figure 4.5. From the fit the value of energy obtained between two levels was obtained, $\Delta E = 0.241(5)$ K. The obtained energy gap is close to the expected value of 0.235 K [84] however from the figure it can be seen that the fit does not fit with the data completely. This shows that there are other competing factors (like magnetic ordering) causing the upturn in the heat capacity of $Nd_3Ga_3Ge_2BeO_{14}$.

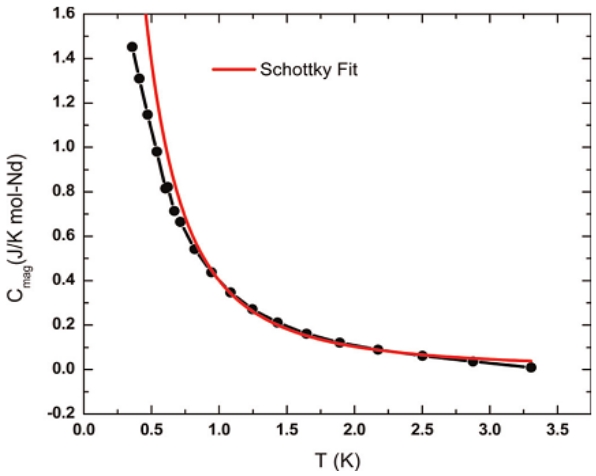

Figure 4.5 Schottky fit to magnetic heat capacity of $Nd_3Ga_3Ge_2BeO_{14}$ as a function of temperature in a 0 T field. [16]

The nature of other competing interactions can be explored by obtaining the total entropy release for the 9 T data by integrating C_{mag}/T as a function of T for a temperature range of base (0.350 K) to 65 K (figure 4.6).

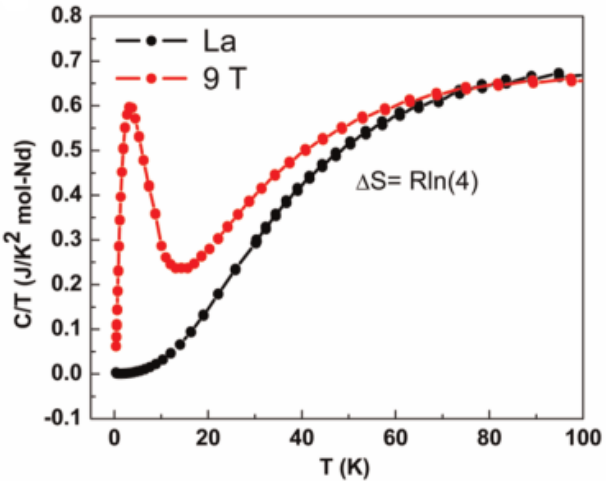

Figure 4.6: Magnetic entropy is obtained by integrating the area between red and black data set for $Nd_3Ga_3Ge_2BeO_{14}$. [16]

The calculated entropy was then used to calculate the number of states w using S = R ln (w). The calculation gave a value of 4.0 (0.1) which is expected for Nd^{3+}. Splitting of the Nd^{3+} J=9/2 state in 5 Kramers doublets is expected in crystal field of the magnetic ion above 77 K with a gap of

6.9 meV between the first two doublets [78]. Thus in this temperature regime, ΔS= R ln (4) is expected from two sets of doublets contributing to the upturn in heat capacity.

4.4 MuSR

MuSR measurements were performed on $Nd_3Ga_3Ge_2BeO_{14}$ to further explore the low temperature magnetism and to confirm the results obtained so far.

4.4.1 Varying Field

Figure 4.7 shows the comparison of the effect of longitudinal field on the asymmetry of the signal as the field was increased from 0.002 to 0.5 T. The 0.002 T field is decoupling the long time asymmetry, but is not strongly affecting the early time parts. The temperature was maintained at 0.024(6) K and the response was collected over time in μS.

The source of relaxation is the dynamic local field at the muon stopping site. The asymmetry (polarization) decay can be exponentially expressed as, $P = e^{-\lambda t}$ in both zero and longitudinal magnetic field.

A stretched exponential relaxation function was used to fit the asymmetry for LF = 0.002 T for the $Nd_3Ga_3Ge_2BeO_{14}$ data.

$$P = e^{(-\lambda t)^{\alpha}} \qquad (4.2)$$

The fit is shown in figure 4.7 (bottom panel). The fit converged successfully and the obtained parameters were the $\lambda = 13\ (3)\ \mu s^{-1}$ and $\alpha = 0.4\ (2)$. A smaller value of α ($\alpha < 1$) is due to multiple stopping sites in langasite [24]. These values further confirm spin dynamics at low temperatures for the langasites when compared with other well studied systems like $Nd_3Ga_5SiO_{14}$ [81]. An increase in asymmetry was observed when field is applied. The difference in zero field

(0.002 T) and field signals is because of the decoupling of spins in the presence of a field. This is an indication of strong exchange interactions [8].

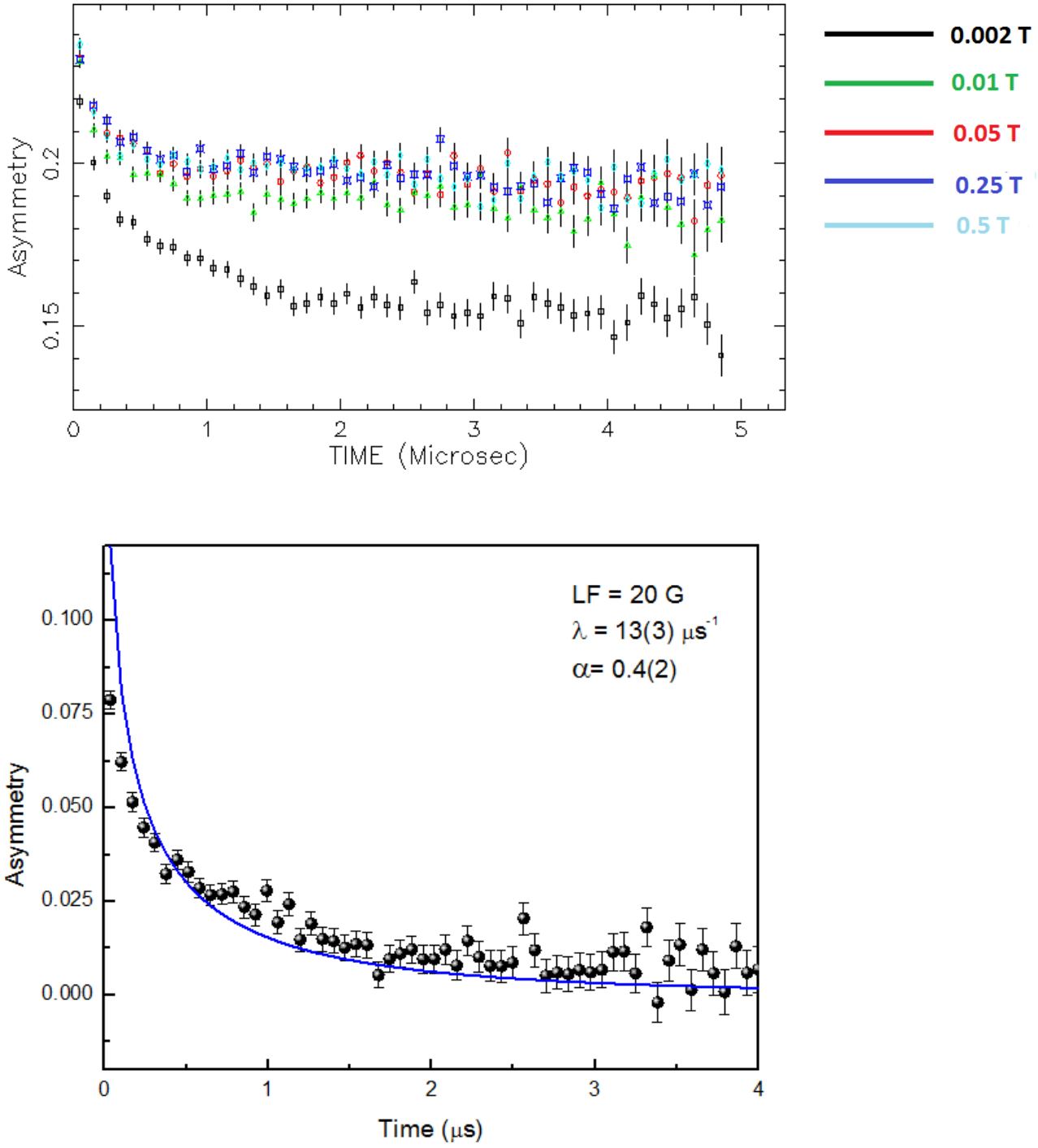

Figure 4.5: (top) Effect of the field on the asymmetry of the signal when longitudinal field was varied from 0.0020 to 0.5000 T. (bottom) Exponential fit performed on the 0.002 T data.

4.4.2 Varying Temperature

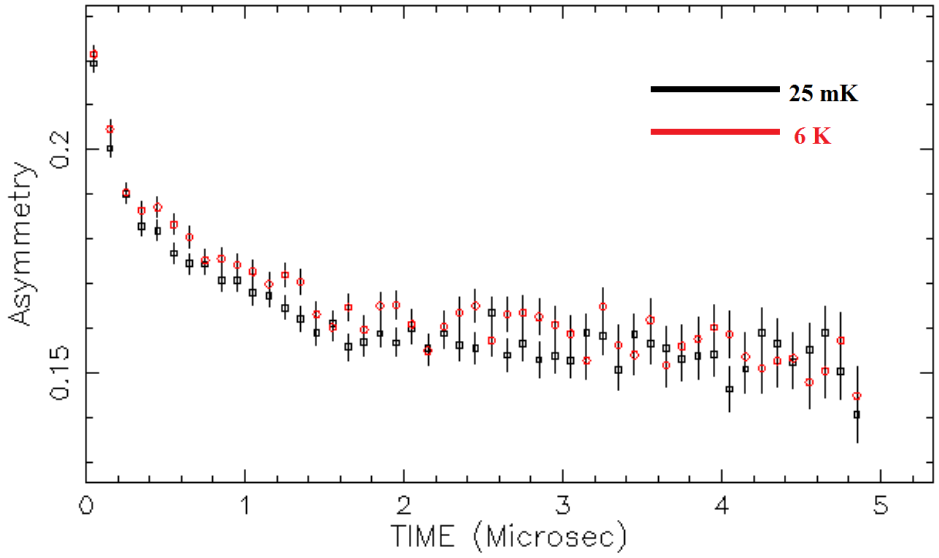

Figure 4.6 Effect of temperature on the asymmetry of the signal when the temperature was varied from 0.025 K to 6 K in a longitudinal field of 0.0020 T.

Figure 4.8 shows the longitudinal field measurements at 0.025 K and 6 K. It can be seen that there is no difference in the asymmetry between 0.025 K and 6 K in zero field, which shows that at least on the time scale that muons are sensitive to, there is no evolution in the magnetism in this temperature range. This means is that there is a decoupling from environmental effects (the silver sample holder, copper in the dilution refrigerator, nuclear moments in the sample) but the magnetism (which is represented by the fast relaxing front end) is not decoupled. The size of the field required to decouple the magnetism is an indicator of how dynamic a sample is. Since it is not decoupled to at least 0.5 T, the system appears to be dynamic down to at least 0.025 K.

4.5 Neutron scattering

4.5.1 Inelastic Neutron Scattering on $Nd_3Ga_3Ge_2BeO_{14}$

For $Nd_3Ga_3Ge_2BeO_{14}$ inelastic neutron scattering measurements were performed to explore the dynamic spin correlations, and the field and temperature dependence of the features. The measurements were performed at 0, 6 and 10 T field strengths for a wavelength of 4.8 Å. The background was subtracted using a 50 K run. In figure 4.9, it can be seen that at the base temperature in zero field, some magnetic diffuse scattering is present close to the elastic channel. Magnetic excitations were also observed at very low energies (less than 0.4 meV). These excitations are of the temperature scale of < 4 K, which is consistent with the low Θ_{CW} for this compound Θ_{CW} << 4 K).

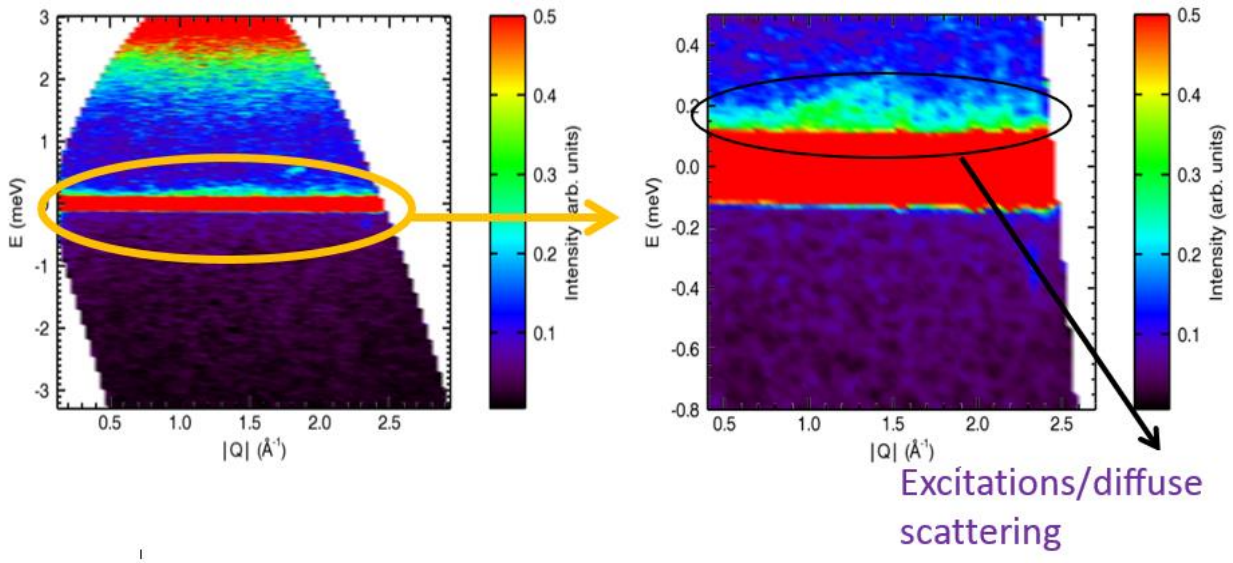

Figure 4.7 Diffuse scattering observed in $Nd_3Ga_3Ge_2BeO_{14}$ close to the elastic channel using the DCS at λ = 4.8 Å in zero field and T= 0.075 K.

In order to see if the excitations are persistent above the base temperature, another run was performed by keeping all parameters same and increasing the temperature to 1.5 K. From figure 4.10 it can be seen that the excitations are clearly visible at 1.5 K.

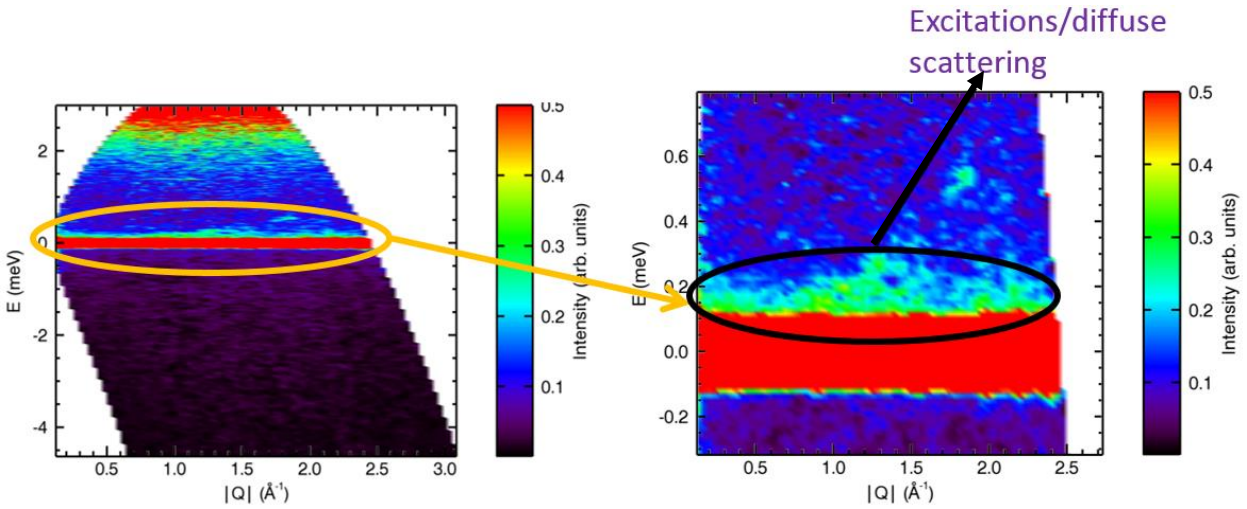

Figure 4.8 Diffuse scattering observed in $Nd_3Ga_3Ge_2BeO_{14}$ close to the elastic channel using the DCS at $\lambda = 4.8$ Å in zero field and T= 1.5 K.

Magnetic diffuse scattering is a result of magnetic interactions between the spins below a certain temperature (Θ_{CW}). Thus an external field should affect the excitations if they are magnetic in nature. Keeping this in mind, the field was increased to 6 T while keeping the temperature and wavelength constant. From figure 4.11 it can be seen that the excitations are suppressed when an external field is applied.

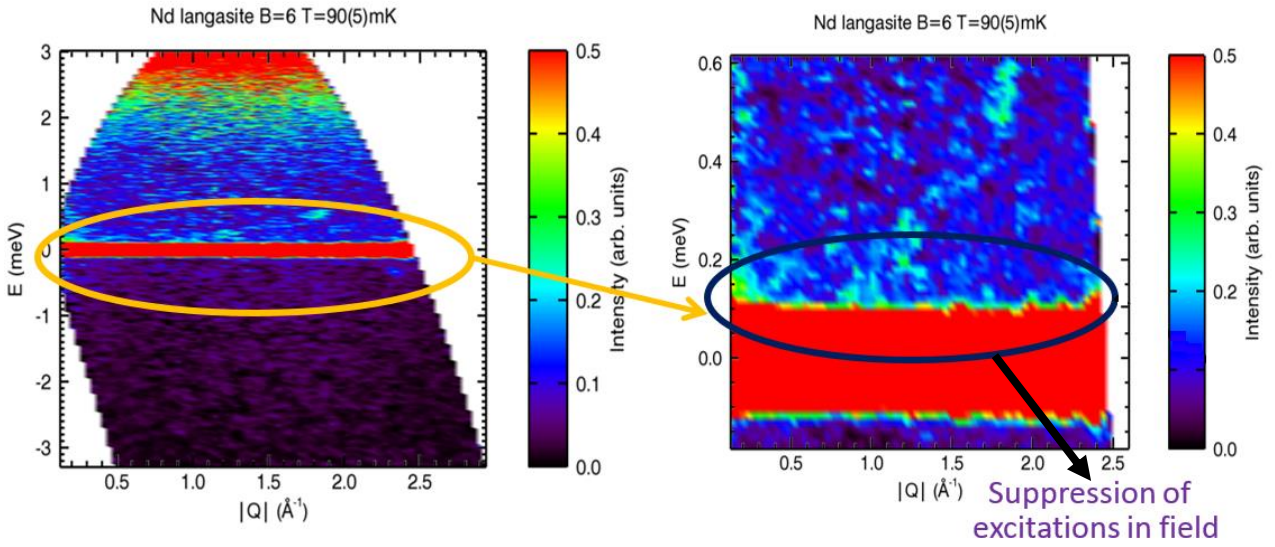

Figure 4.9 Further suppression of excitations observed in $Nd_3Ga_3Ge_2BeO_{14}$ close to the elastic channel using the DCS at $\lambda = 4.8$ Å when B = 6 T is applied at T= 0.090 K.

When the strength of the field was increased to 10 T, a further suppression of excitations was observed.

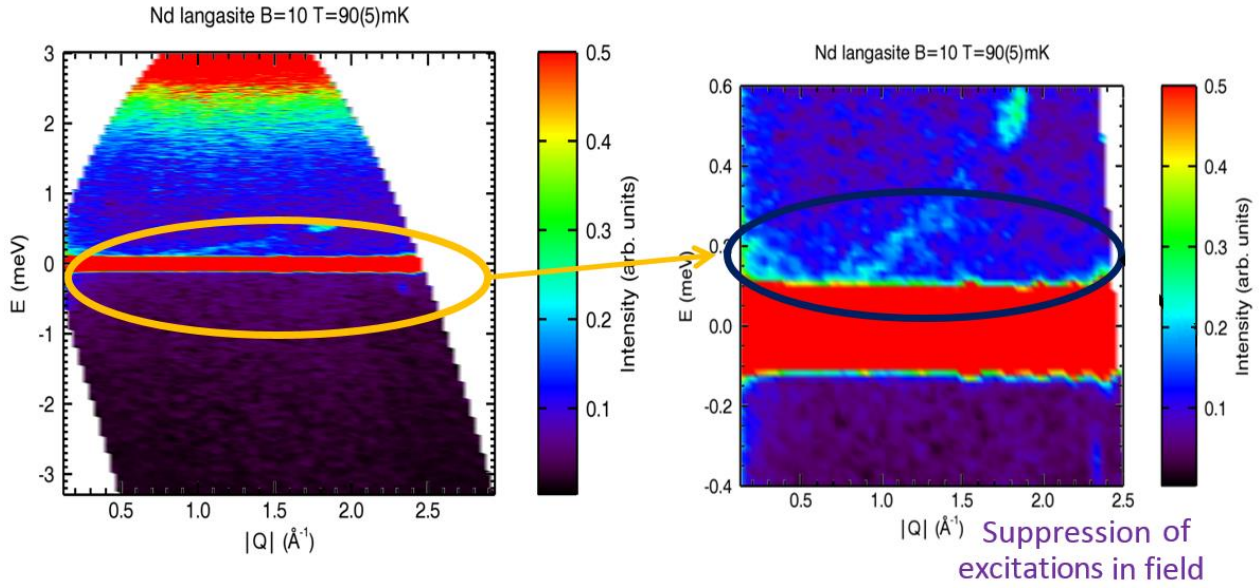

Figure 4.10 Suppression of excitations observed in $Nd_3Ga_3Ge_2BeO_{14}$ close to the elastic channel using the DCS at $\lambda = 4.8$ Å when B = 10 T is applied at T= 0.090 K.

Figure 4.13 shows a comparison between the different fields. Suppression of diffuse scattering can be clearly seen. From this data it can be concluded that Nd-langasite shows evidence of diffuse scattering from the base to at least 1.5 K.

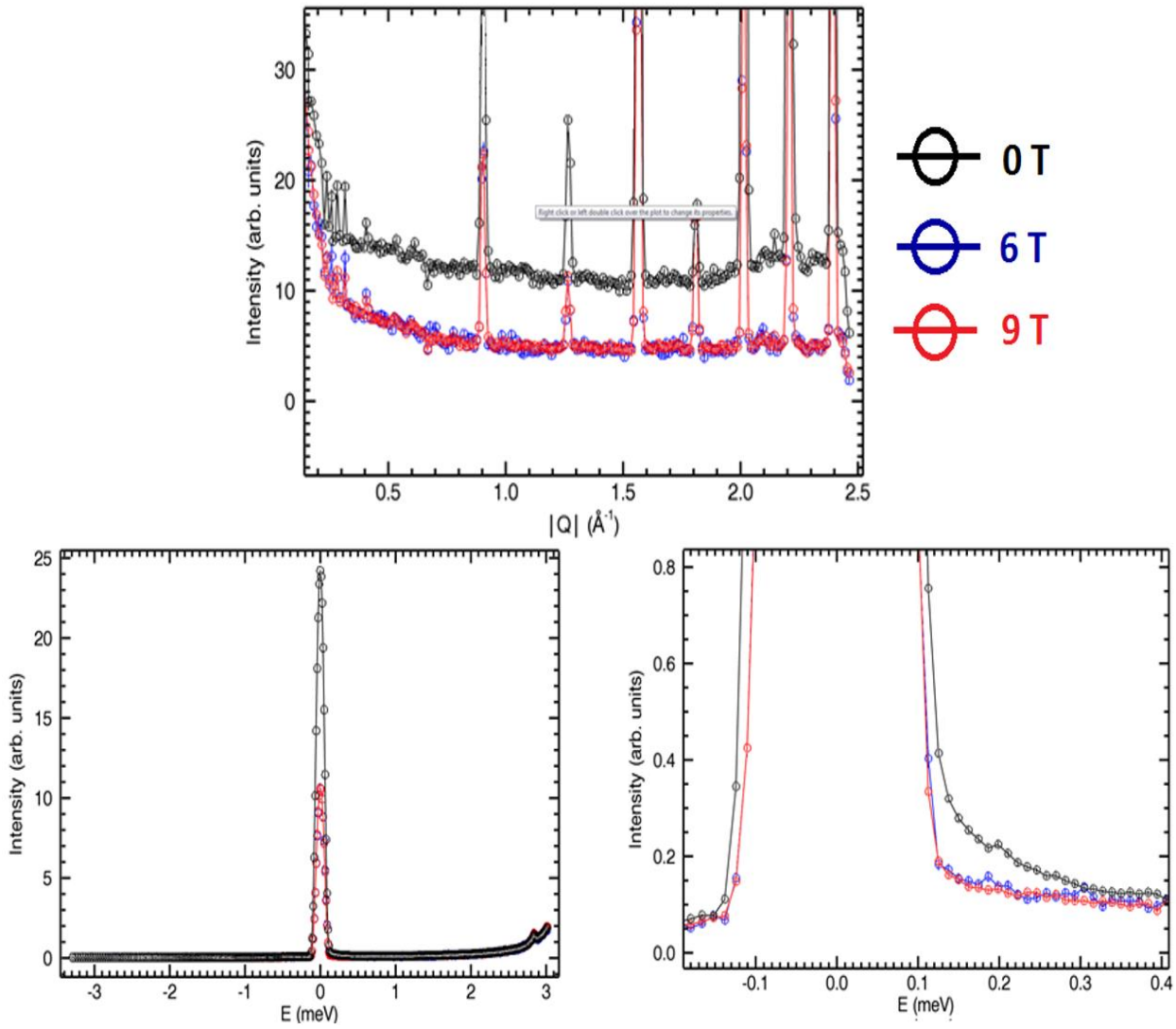

Figure 4.11 Figure 82: Field dependence of inelastic neutron scattering data for $Nd_3Ga_3Ge_2BeO_{14}$at T=0.070(10) K with field strengths of 0, 6 and 9 T (top- integration over Q for E [-0.5,0.5meV].

4.5.5.1 Form Factor Fit for $Nd_3Ga_3Ge_2BeO_{14}$

The nature of diffuse scattering can be analyzed further by performing a spin liquid form factor fit. The F^2 (form factor) for Nd for a certain Q range is given by the polynomial

$$F(Q) = 1.0082(0.0084) - 0.01122(0.00898)Q - 0.03306(0.00266)\,Q^2 + 0.00265(0.00021)Q^3 \quad (4.3)$$

The diffuse scattering was obtained by subtracting the 9 T data from 0 T data. It can be noted that the Bragg peaks are still present and might interfere with the fit so the data must be corrected for that before performing the fit. The fit was performed by plotting intensity / (form factor)^2 as a function of Q for the range 0 to 2 $Å^{-1}$. The data was then fit to the sine function given below with fitting parameters A, B and $r_{i,j}$.

$$I(Q) \sim \Sigma_{i,j} < S_i \cdot S_j > \frac{\sin(Qr_{i,j})}{(Qr_{i,j})} \sim A\frac{\sin(Qr_{i,j})}{(Qr_{i,j})} + B \quad (4.4)$$

The obtained fit is shown in figure 4.14 and it can be seen that the fit converges for the Q range. The parameters obtained for the fit are as follows

Table 4.1 Table showing the parameters obtained from the form factor fit (equation 4.2)

A	B	$r_{i,j}$
-2(1)	7(1)	4.8 (5)

A negative value of A shows that the nearest neighbour spin correlations are antiferromagnetic in nature. Also B is the offset and $r_{i,j}$ is the nearest neighbour distance. The obtained value for $r_{i,j}$ was 4.8 (5) Å. This is in close agreements to the numbers obtained for Nd^{3+}- Nd^{3+} nearest neighbour distance for $Nd_3Ga_3Ge_2BeO_{14}$ (4.2 Å) using a Rietveld refinement.

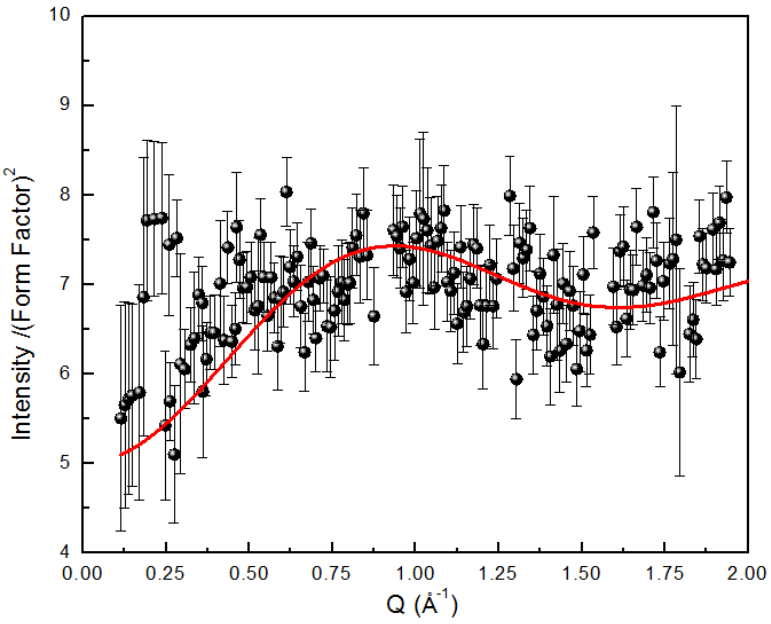

Figure 4.12 Form factor fit for the inelastic scattering obtained for $Nd_3Ga_3Ge_2BeO_{14}$ at the DCS at 0.075 K.

Thus it can be concluded that the net interactions are antiferromagnetic in nature and the spin correlation is limited to the corners of the Kagomé lattice.

4.5.2 Diffuse Scattering on $Nd_3Ga_3Ge_2BeO_{14}$

The temperature dependence of the magnetic response of $Nd_3Ga_3Ge_2BeO_{14}$ was measured at the ILL using the D7 spectrometer. The data was collected at 0.035 K, 1.2 K, 10K and 40 K. The 40 K data was used to subtract the background contributions. Figure 4.15 shows the results for a Q range of 0 to 2.5 Å^{-1}. It can be seen that there are excitations present at 0.035 K and 1.2 K which get suppressed as the temperature is increased to 10 and eventually 40 K. This is in agreement with the results obtained using the inelastic neutron scattering at DCS for this sample. The

diffuse scattering is present at a base temperature of 0.035 K up to 1.2 K and vanishes as the temperature is increased. This indicates magnetic ordering as the temperature is reduced below 1.2 K and hints towards spin liquid like interactions at low temperatures.

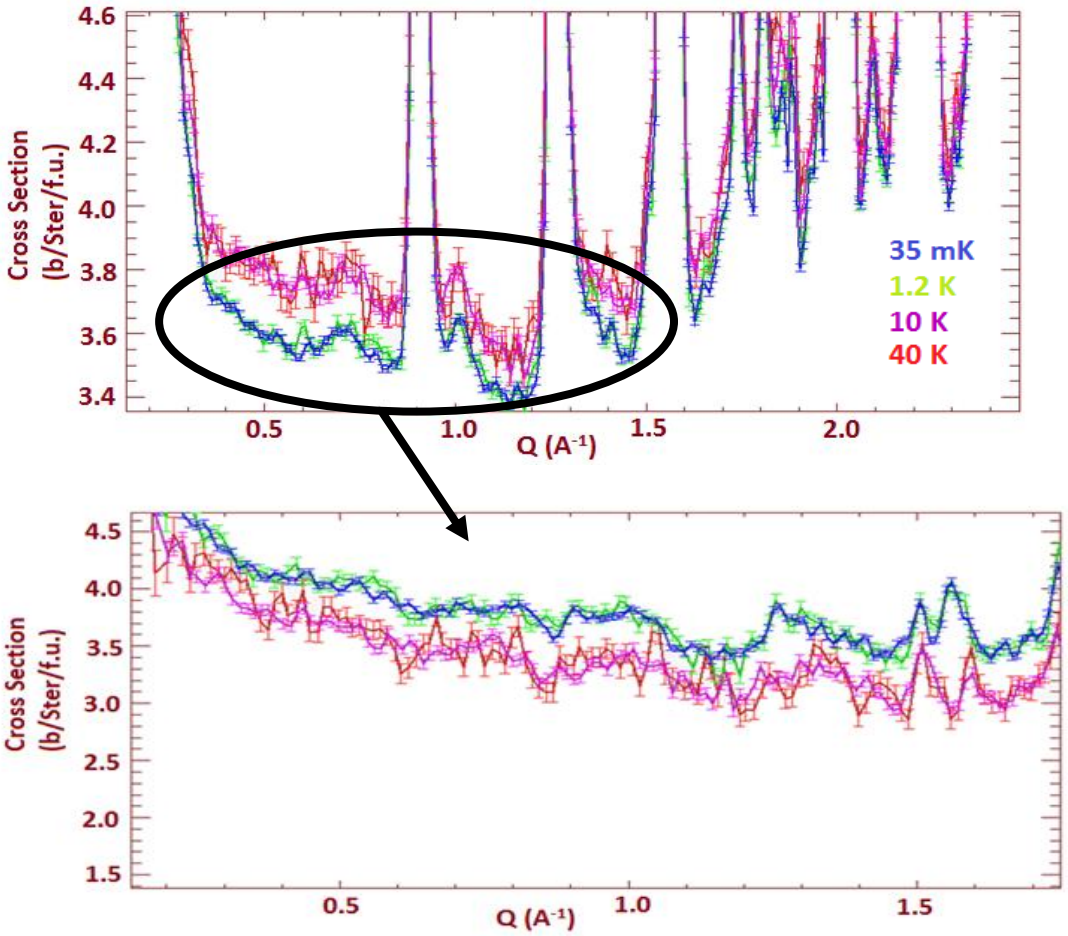

Figure 4.13 Temperature dependence of polarized neutron scattering data for $Nd_3Ga_3Ge_2BeO_{14}$ obtained at 0.035 K, 1.2 K, 10 K and 40 K. The top panel shows origin of diffuse scattering as the temperature approaches 1.2 K and 0.035 K. The bottom panel clearly shows diffuse scattering after subtracting out the Bragg peaks.

4.5.2.1 Flipping Ratio

In neutron scattering, the flipping ratio is defined as the ratio of cross section of neutron beam parallel and antiparallel to magnetization of the system [85] .

$$P = \frac{N_+ - N_-}{N_+ + N_-} = \frac{(N_+/N_-) - 1}{(N_+/N_-) + 1} = \frac{F - 1}{F + 1} \tag{4.5}$$

Advantages of analyzing the flipping ratio include the cancellation of systematic errors [85] and sensitivity to weak magnetic scattering.

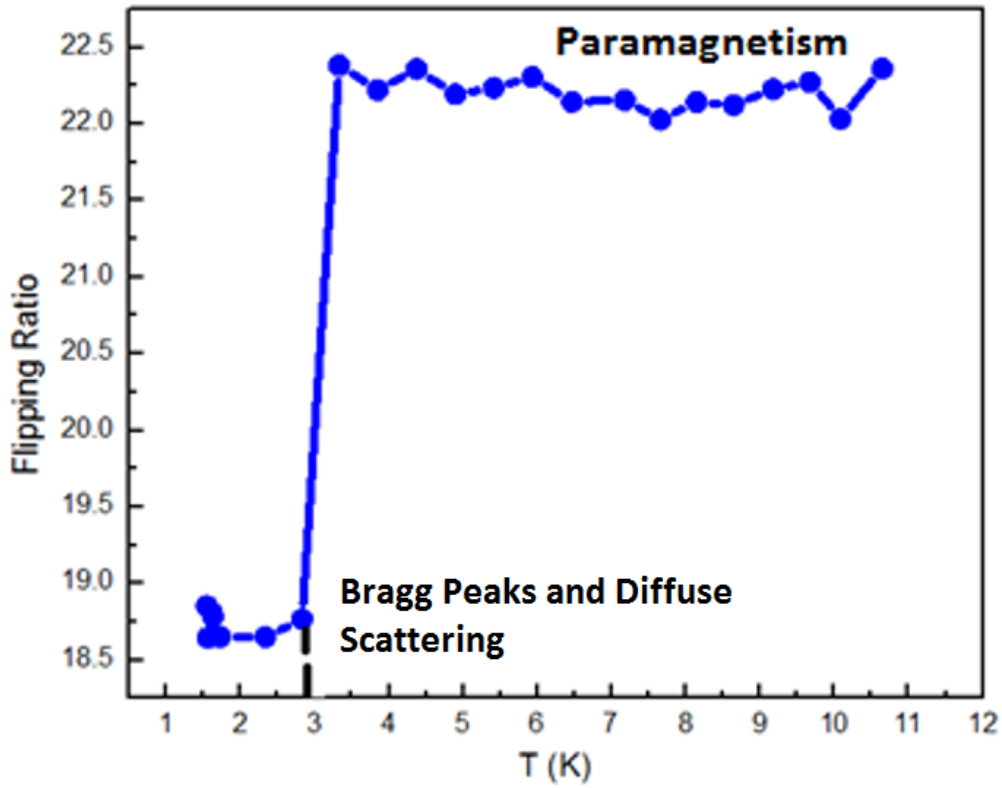

Figure 4.14 Flipping ratio plotted as a function of temperature for $Nd_3Ga_3Ge_2BeO_{14}$. A change in character of the scattering can be seen around 3 K.

The flipping ratio was plotted as a function of temperature as can be seen in figure 4.16. Between 3 and 11 K, the sample exhibits paramagnetism. However, a sharp drop is observed close to 3 K. Below this temperature the sample shows signs of diffuse scattering which is consistent with the results obtained using other physical property measurements. Thus for $Nd_3Ga_3Ge_2BeO_{14}$, the ILL results show magnetic diffuse scattering which changes character around ~3 K. This also gives rise to magnetic Bragg peaks. There is a possibility of a ferromagnetic component which will be explored further in future work.

4.6 Summary

The results obtained for $Nd_3Ga_3Ge_2BeO_{14}$ can be summarized as follows

- Weak antiferromagnetic interactions are clearly seen with an observed $\Theta_{CW} \sim$ - 0.16 K.
- Neutron scattering and MuSR data did not show any evidence of magnetic long range ordering in the sample.
- Broadening of heat capacity peak with the increase in magnetic field strength could be due to short range ordering in the compound.
- Diffuse scattering is evident from the inelastic neutron data and is prominent below 1.2 K which indicates that the magnetic correlations are limited to nearest neighbours.

Chapter 5

Magnetism of $Pr_3Ga_3Ge_2BeO_{14}$

5.1 D.C. Susceptibility

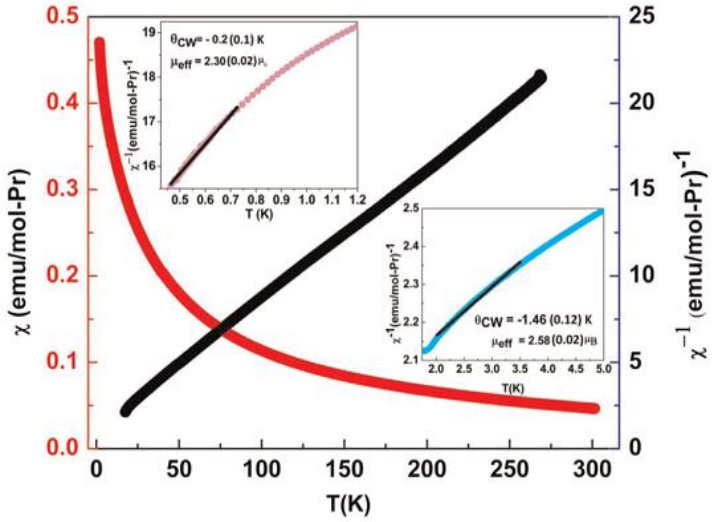

Figure 5.1 Magnetic susceptibility and inverse susceptibility as a function of temperature (inset: Curie–Weiss fits) for $Pr_3Ga_3Ge_2BeO_{14}$ [16].

D.C. susceptibility (red) and inverse d.c. susceptibility (black) for $Pr_3Ga_3Ge_2BeO_{14}$ as a function of temperature is shown in figure 5.1. A complete overlap between field cooled and zero field cooled measurements was observed thus confirming no glassiness or phase transitions. The magnitude of calculated θ_{CW} suggests the influence of crystal field levels at high temperatures. Thus the fits were limited to the low temperature region (below 8 K). The Curie-Weiss temperature obtained for 1.8 K to 8 K fits was -1.46(0.12) K and the effective magnetic moment was calculated as 2.58(0.02) μ_B which is close to the theoretically calculated value for Pr^{3+}. For fits between 0.500 K and 1.8K, the Curie-Weiss temperatures and effective moments obtained were -0.2(0.1) K and 2.30(0.02) μ_B. It can be observed that the magnitude of Θ_{CW} is small which hints at competing interactions (for example, ferromagnetism) at low temperatures. Thus for

$Pr_3Ga_3Ge_2BeO_{14}$, a clear presence of antiferromagnetic interactions can be seen however the strength of interactions appear to be weaker as compared to $Nd_3Ga_3Ge_2BeO_{14}$.

5.2 Magnetization

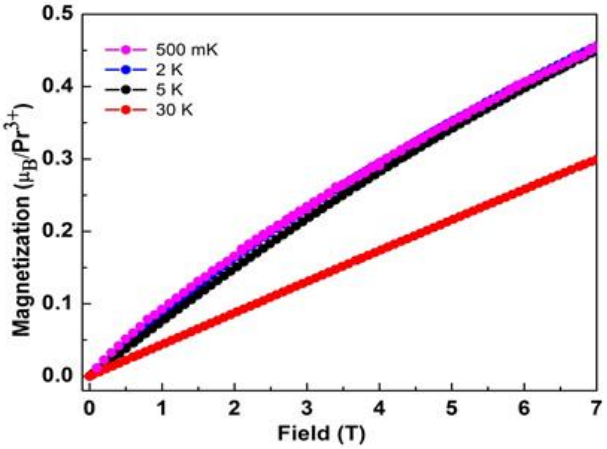

Figure 5.2 Magnetization curves for $Pr_3Ga_3Ge_2BeO_{14}$ at 0.500 K 2 K, 5 K and 30 K in up to 7 T field [16].

Figure 5.2 shows the magnetization of $Pr_3Ga_3Ge_2BeO_{14}$ at 0.500 K 2 K, 5 K and 30 K. From the figure it can be seen that there is no hysteresis present in the measurements thus ruling out any possibility of a ferromagnetic transition. The magnitude of the magnetization increases as the temperature is reduced from 30 to 5 K. But with any further decrease in temperature, the magnetization remains the same. Thus below 5 K all the spins are aligned and any further reduction does not change the alignment. Also since the moment does not reach saturation, it can be assumed that the spins are still in a disordered state.

5.3 Heat Capacity

Figure 5.3 shows the heat capacity (C) of $Pr_3Ga_3Ge_2BeO_{14}$ as a function of temperature (T) and C/T vs T. It can be seen from the plots that there is no evidence of magnetic long range order down to 0.350 K.

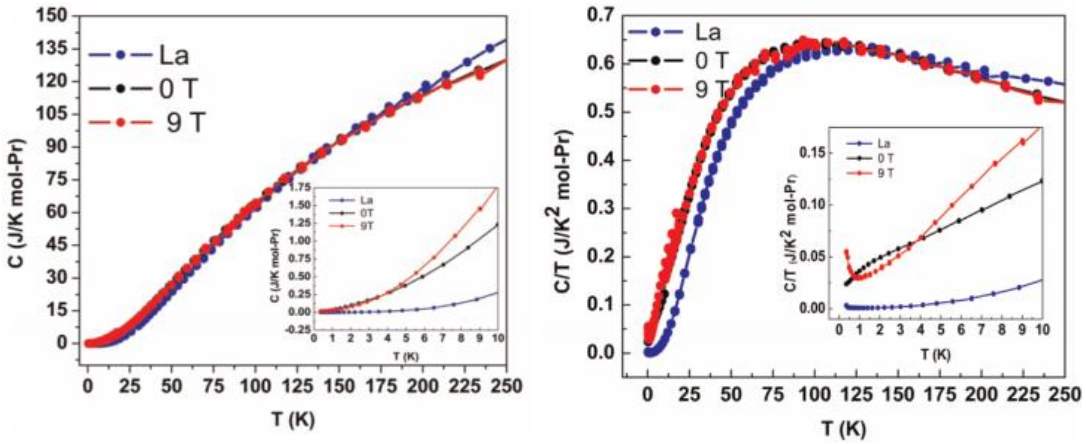

Figure 5.3 Heat capacity as a function of temperature at 0 T, 9 T and lattice standard for $Pr_3Ga_3Ge_2BeO_{14}$ (left) and C/T vs. T data (right) (inset: low T region zoomed in) [16].

The low temperature heat capacity data can be further analyzed by plotting log C_{mag} vs. log T and finding the slope. It was found that the slope has a value of 2.03 (0.05) which indicates a T^2 ($C_{mag} = \gamma T^2$) dependence of the heat capacity (figure 5.4).

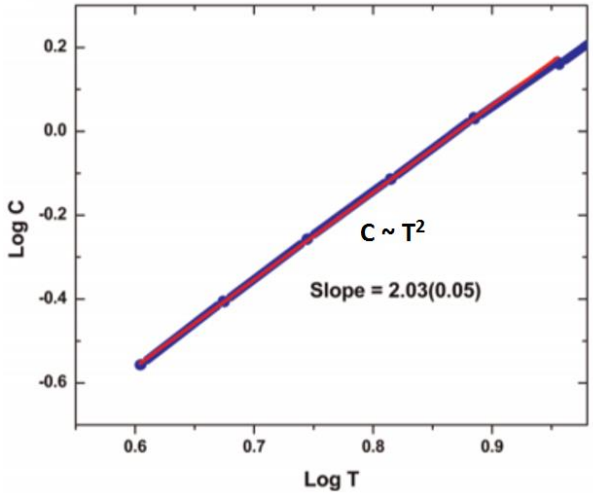

Figure 5.4 T^2 dependence of heat capacity for $Pr_3Ga_3Ge_2BeO_{14}$[16]

This T^2 dependence can be interpreted as being due to short ranged 2D magnetic correlations typical of disordered spins on the Kagomé lattice [77]. Zero field heat capacity measurement showed an increase in C_{mag} with decreasing temperature which shifted to higher temperatures in

a field. This feature was predicted to be nuclear in origin based on the nuclear energy level scheme of Pr^{3+} [77]. The strong T^2 dependence of the magnetic component of the heat capacity for $Pr_3Ga_3Ge_2BeO_{14}$ suggests that 2D dynamic correlations are present at low temperatures. The absence of long range order and T^2 dependence of magnetic heat capacity are strong evidence for a quantum spin liquid ground state down to 0.350 K.

5.4 Neutron Scattering

5.4.1 Elastic Neutron Scattering Measurements on $Pr_3Ga_3Ge_2BeO_{14}$

The temperature dependence of the response of the sample was studied using λ =4.8 Å. Measurements were performed at 0.070 K, 0.500 K, 1.5 K, 10 K and 50 K. As the temperature was increased from 0.070 K to 50 K, no change in the inelastic signal was observed. The intensities of the Bragg peaks remain the same as the temperature is decreased and no new Bragg peaks appeared. Thus there is no evidence of magnetic long range ordering in the Pr langasite.

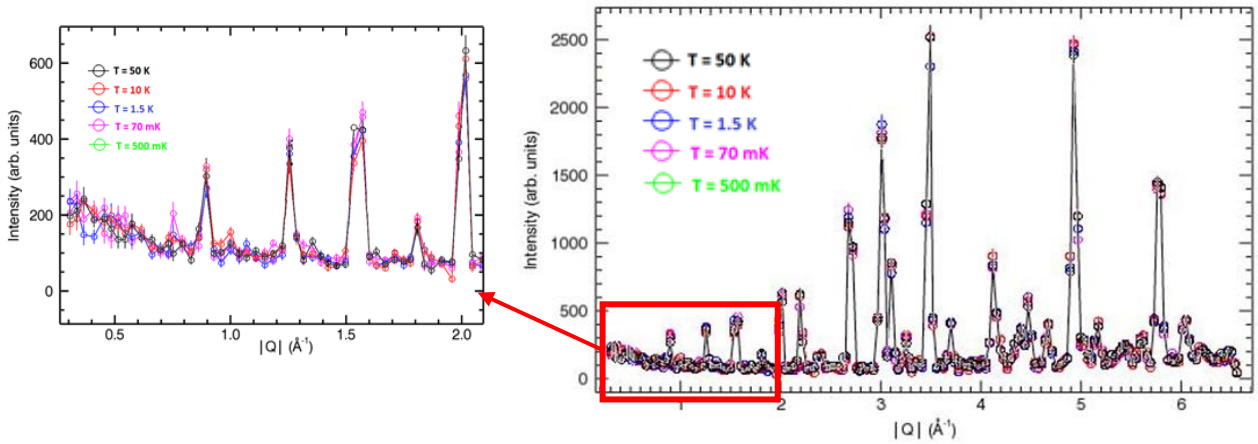

Figure 5.5 Elastic neutron scattering obtained for $Pr_3Ga_3Ge_2BeO_{14}$ as a function of temperature for 0.500 K, 0.070 K, 1.5K, 10 K and 50 K obtained at the DCS. (left) zoomed in 0 <Q <2 $Å^{-1}$. (λ = 4.8 Å)

5.5 Summary

- $Pr_3Ga_3Ge_2BeO_{14}$ shows weak antiferromagnetic interactions with a $\Theta_{CW} \sim -0.2$ K.
- There was no evidence of magnetic long range ordering.
- $C \sim T^2$ relation at low temperatures indicates 2-D magnetic correlations in this compound.

Chapter 6

Magnetism of $Sm_3Ga_3Ge_2BeO_{14}$

6.1 D.C. Susceptibility

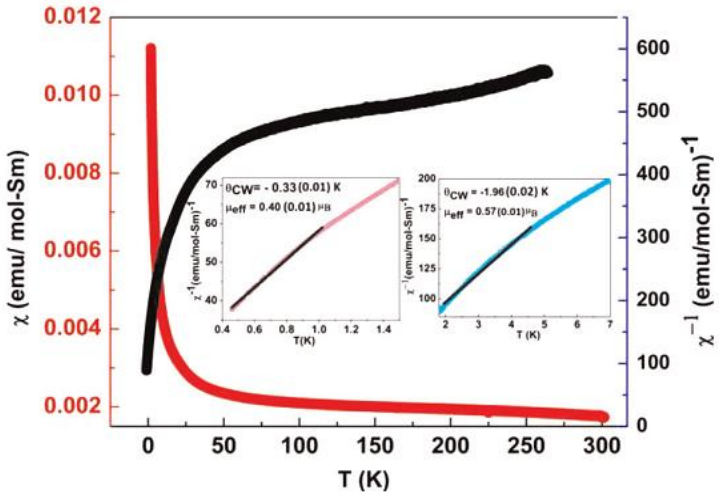

Figure 6.1 Magnetic susceptibility and inverse susceptibility as a function of temperature (inset: Curie–Weiss fits) for $Sm_3Ga_3Ge_2BeO_{14}$ [16].

The d.c. magnetic susceptibility of $Sm_3Ga_3Ge_2BeO_{14}$ is shown in figure 6.1 (red) for a temperature range of 0.350 to 300 K. The black data set shows the inverse d.c. susceptibility as a function of temperature. A steep rise is observed between base and 50 K in the inverse susceptibility data set and over 50 K the rise is not as substantial. This broad anomalous feature above 50 K can be attributed to the population of higher crystal fields at high temperature in this langasite. A similar feature has been observed for the pyrochlore $Sm_2Ti_2O_7$ where a temperature dependence of the susceptibility can be seen with a broad maximum at 140 K [86]. The Curie-Weiss fits were done at different temperature ranges and the Curie-Weiss temperatures (θ_{CW}) and effective moments were calculated. Above 50 K, a θ_{CW} of -1133(2) K and a μ_{eff} of 4.54 (0.01) μ_B was obtained. The numbers are unrealistic and they confirm the initial prediction of crystal field population at higher temperatures. Low temperature fits for $Sm_3Ga_3Ge_2BeO_{14}$ were also attempted. For the temperature range of 1.8K to 8 K (Figure 6.1 (blue, inset)) the θ_{CW} and μ_{eff}

obtained were -1.96(0.01) K and 0.57(0.01) μ_B and for 0.500 K to 1.8 K (Figure 6.1 (pink, inset)), θ_{CW} = - 0.33(0.02) K and μ_{eff} = 0.40(0.01) μ_B. The effective moment of a free Sm ion is 0.84 μ_B [54]. The d.c. susceptibility measurement on $Sm_3Ga_3Ge_2BeO_{14}$ confirmed that the Sm spins have a net antiferromagnetic interactions. The obtained values from the low temperature fit are smaller than expected which indicates that the Sm ion is interacting with the neighbouring Sm ions.

6.2 Magnetization

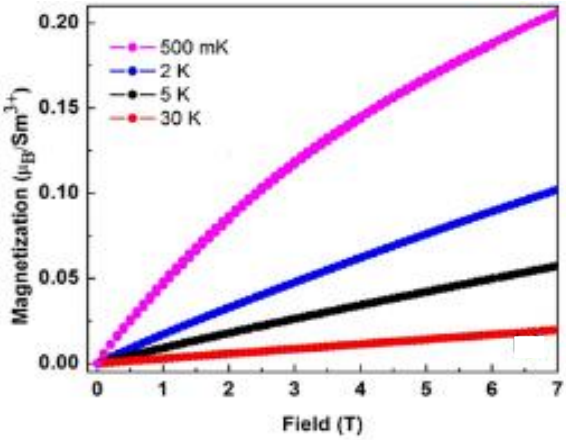

Figure 6.2 Magnetization curve for $Sm_3Ga_3Ge_2BeO_{14}$ at 0.500 K, 2 K, 5 K and 30 K in up to 7 T field [16].

Figure 6.2 shows the magnetization of $Sm_3Ga_3Ge_2BeO_{14}$ as a function of field at 0.500 K, 2, 3 and 30 K. The magnitude of magnetization per Sm ion is much smaller than expected which shows that the material is magnetically more disordered than $Pr_3Ga_3Ge_2BeO_{14}$ and $Nd_3Ga_3Ge_2BeO_{14}$. A clear trend can be seen in the magnetization as the temperature is decreased from 30 K to 0.500 K. At 0.500 K, the magnetization increase significantly which shows that more spins order as the temperature is reduced. The magnetization does not reach saturation even in the presence of a strong field at low temperatures which indicates that there is an absence of long range ordering.

6.3 Heat Capacity

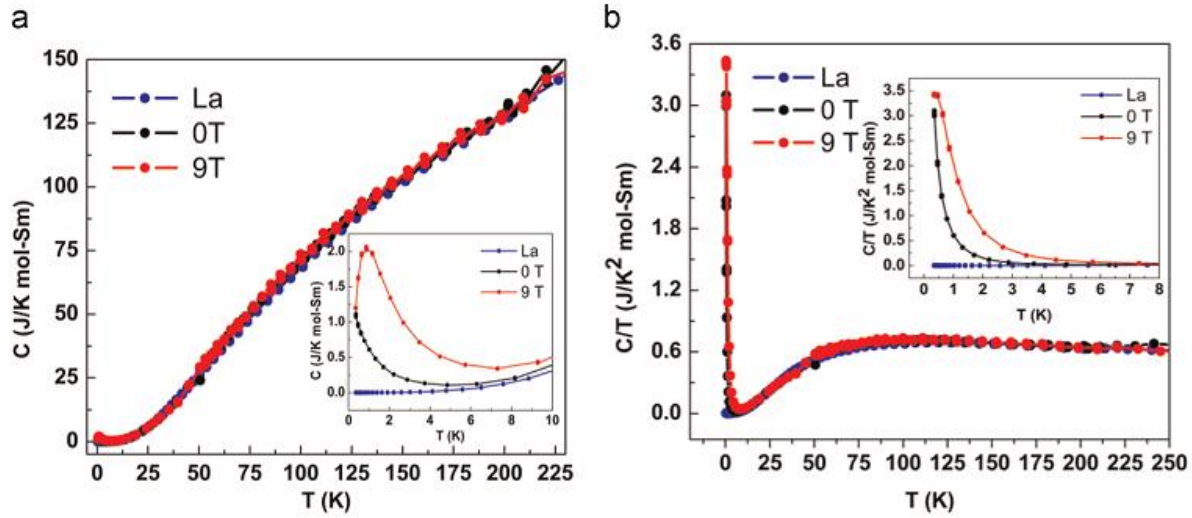

Figure 6.3 : Heat capacity as a function of temperature at 0 T and 9 T and lattice standard for $Sm_3Ga_3Ge_2BeO_{14}$ (left) C/T vs. T data (right) (inset: low T region zoomed in) [16].

Figure 6.3 shows heat capacity measurements performed on $Sm_3Ga_3Ge_2BeO_{14}$ for a temperature range of 0.350 to 300 K in 0 and 9 T fields. Figure 6.3 (a) shows the comparison between the lattice standard, 0 T and 9 T measurements. As expected, for the lattice standard the heat capacity reaches zero as the temperature approaches zero. For $Sm_3Ga_3Ge_2BeO_{14}$, in 0 T an increase in the heat capacity was observed below 4 K. When 9 T field is applied, this peak broadens and shifts to higher temperatures. This typically is a feature of a Schottky anomaly but the Schottky fit did not converge in this case indicating that there are other factors contributing to this behaviour of the data. Figure 6.3 (b) shows the C/T vs T plot. From the figure it can be seen that a complete peak is not obtained even in 9 T so the full entropy calculations cannot be performed.

For Sm^{3+} containing compounds, the specific heat consists of contributions from nuclear terms, the lattice and magnetic terms. The nuclear component is typically significant below 0.4 K as in $Sm_2Ti_2O_7$[87]. The broad feature observed over 25 K is due to the crystal field terms at higher

temperature and was also visible in the d.c. susceptibility measurements. Heat capacity measurements on $Sm_3Ga_3Ge_2BeO_{14}$ clearly indicated the presence of magnetic correlations at low temperature but even lower temperature heat capacity data (below 0.350 K) is required to make conclusions.

6.4 Summary

- Weak antiferromagnetic interactions can be observed with a Θ_{CW} ~ -0.33 K.
- No sign of magnetic ordering was observed in zero field.
- A low temperature peak emerges in an applied field in heat capacity which might indicate a long range ordering in an applied magnetic field.
- Neutron scattering measurements were not completed due to the highly absorbing nature of Sm with respect to the thermal neutrons.

Chapter 7

Magnetism of $Eu_3Ga_3Ge_2BeO_{14}$

7.1 D.C. Susceptibility

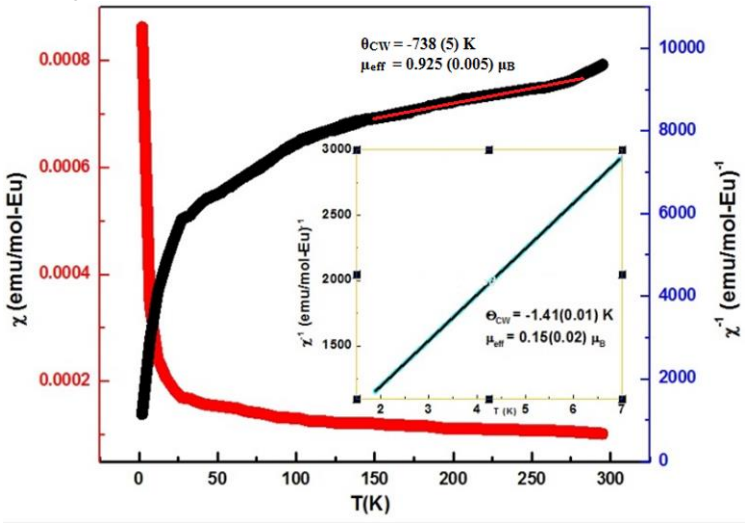

Figure 7.1 Magnetic susceptibility and inverse susceptibility as a function of temperature (inset: Curie–Weiss fits) for $Eu_3Ga_3Ge_2BeO_{14}$.

D.C. susceptibility and inverse as a function of temperature for $Eu_3Ga_3Ge_2BeO_{14}$ is shown in figure 7.1. For Eu, a high temperature fit (150-300 K) gave a θ_{CW} of -738(5) K and a μ_{eff} of 0.925 (0.005) μ_B. The magnitude of θ_{CW} is very high and is unrealistic. A low temperature fit for the temperature range of 1.8 K to 8 K gave a θ_{CW} of -1.41(0.01) K and μ_{eff} of 0.15(0.02) μ_B. The θ_{CW} confirms net antiferromagnetic interactions of the system and μ_{eff} indicates towards the presence of very small but non-zero net magnetic moment. A broad feature in the inverse susceptibility vs temperature (black data set) is similar to that observed in case of $Sm_3Ga_3Ge_2BeO_{14}$. Sm and Eu both exhibit Van Vleck paramagnetism and this broad feature might be result of that. The magnitude of the susceptibility is also very low as compared to Nd, Pr and Sm members of the family which shows a very weak magnetism.

7.2 Magnetization

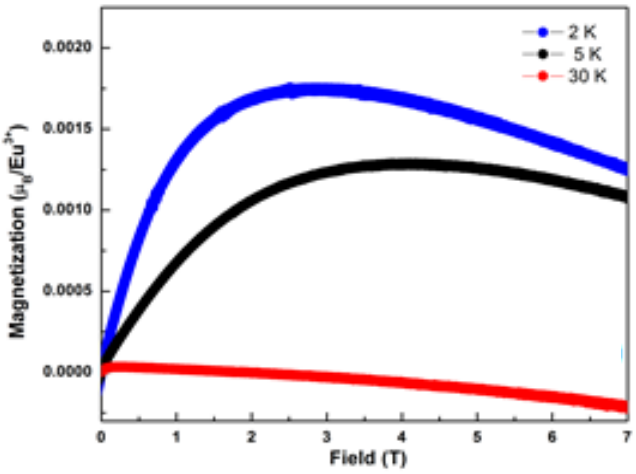

Figure 7.2 Magnetization curve for $Sm_3Ga_3Ge_2BeO_{14}$ at 0.500 K, 2 K, 5 K and 30 K in up to 7 T field.

For the Eu-langasite, the magnetization as a function of field was obtained from 0 to 7 T at three different temperatures of 2, 5 and 30 K. For all three measurements it was seen that the magnetization reaches a maximum and when the field is applied any further, the value of the magnetization decreases. At 30 K, the value drops below zero which is not realistic. This drop might be because of the singlet state of Eu in this compound. The magnetism of the Eu containing compounds can be compromised if the singlet state is more stable as compared to triplet. Magnetism of Eu has been studied in different classes of compounds before but a behaviour like this has not been observed so far. Thus a comparison cannot be made with the ground state of the Eu-langasite with the other Eu containing compounds at this stage. The behaviour is likely due to the singlet state of Eu ion and the downturn in magnetization might be because of a higher crystal field transition.

7.3 Heat Capacity

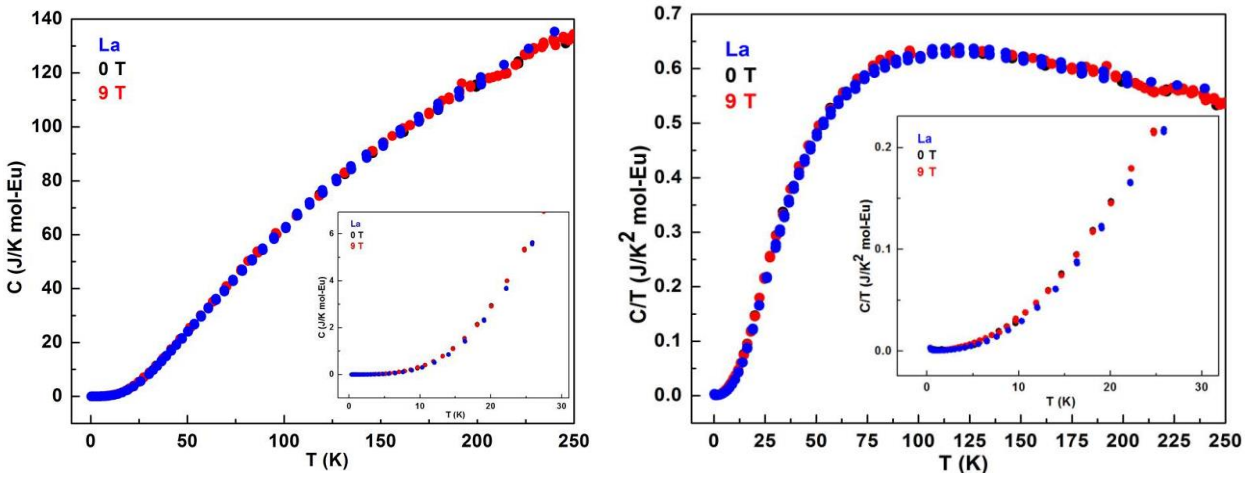

Figure 7.3 Heat capacity as a function of temperature at 0 T and 9 T and lattice standard for $Eu_3Ga_3Ge_2BeO_{14}$ (left) C/T vs. T data (right) (inset: low T region zoomed in)

Heat capacity measurements were performed on $Eu_3Ga_3Ge_2BeO_{14}$ to further understand the ground state and the magnetism of this langasite. The measurements were performed from 0.350 K to 300 K in 0 and 9 T fields. The heat capacity appeared to have no contribution from the magnetism of the sample. The 0 and 9 T data highly resembled the heat capacity of the lattice standard $La_3Ga_3Ge_2BeO_{14}$. This measurement suggests the presence of a singlet ground state of Eu in this langasite which was also evident from the d.c. susceptibility and magnetization data. Thus this material was not analyzed further for its low temperature magnetism.

7.4 Summary

- The Eu^{3+} ion commonly exists in a singlet state.
- Magnetic characterization of the $Eu_3Ga_3Ge_2BeO_{14}$ was inconclusive.
- No magnetism effects were observed in the heat capacity measurements.

Chapter 8

Conclusions and Future Directions

8.1 Conclusions

Taking inspiration from the previously studied langasites $Pr_3Ga_5SiO_{14}$ and $Nd_3Ga_5SiO_{14}$, four Be-langasites $A_3Ga_3Ge_2BeO_{14}$ (A = Pr, Nd, Sm and Eu) and a lattice standard $La_3Ga_3Ge_2BeO_{14}$ were synthesized. The synthesis was done using a solid state ceramic method at high temperatures. These compounds were further analyzed using X-ray diffraction, Rietveld refinements and bond valence analysis which confirmed the phase purity, stability and oxidations states of the ions of the langasite phase in this substitution. The series was expanded until the Eu member as the langasite stability field collapses for ion sizes smaller than Eu. These compounds were further characterized by physical property measurements like magnetization, magnetic susceptibility and heat capacity. The magnetization measurements do not show any hysteresis in any of the four magnetic compounds. Curie-Weiss fits to the magnetic susceptibility data yielded negative Curie-Weiss temperatures for all langasites in the low temperature regime. A low temperature region was selected for these fits as at higher temperatures crystal field effects mask the true Curie-Weiss terms. A negative Curie-Weiss temperature indicated the presence of net antiferromagnetic interactions for all of these compounds at low temperatures.

Temperature Range →	**0.500 K to 1.8 K**	**1.8 K to 8 K**	**High T (8 K to 300 K)**
$Pr_3Ga_3Ge_2BeO_{14}$	-0.2 (0.1) K	-1.5 (1) K	-39.9 (2) K
$Nd_3Ga_3Ge_2BeO_{14}$	-0.16 (0.01) K	-1.02 (0.01) K	-37.78 (0.03) K
$Sm_3Ga_3Ge_2BeO_{14}$	-0.33 (0.02) K	-1.96 (0.01) K	-1133 (2) K
$Eu_3Ga_3Ge_2BeO_{14}$	---------	-1.41 (0.01) K	-738 (5) K

No evidence of long range magnetic ordering was observed in all four langasites. For the Nd-langasite, evidence of a dynamic state was observed using the MuSR measurements close to the base temperature (0.090 K). In the presence of a field, a decoupling of spins is observed which shows that the interactions are magnetic in nature. The disordered nature of spins was further confirmed by the presence of diffuse scattering in 0 T from 10 K all the way to the base temperature (0.075 K). Polarized neutron scattering data obtained at the ILL indicates a coexistence of a paramagnetic state along with magnetic short range ordering. More experiments are needed, however, to prove this. The coexistence of paramagnetic and antiferromagnetic state in the Nd-langasite also explains the unsuccessful attempt to fit the low T data to Schottky anomaly for Nd-langasite. All the measurements above suggest that these langasites (except $Eu_3Ga_3Ge_2BeO_{14}$) can be added to the list of spin liquid candidates based on the presence of dynamic correlations at low temperatures and presence of spin liquid like features in the physical property measurement.

8.2 Future Directions

A better understanding of the low temperature interactions is required to classify the compounds as spin liquids. In the future, the first step would be to synthesize new members belonging to the langasite series with ions smaller than Eu occupying the A site in $A_3Ga_3Ge_2BeO_{14}$.

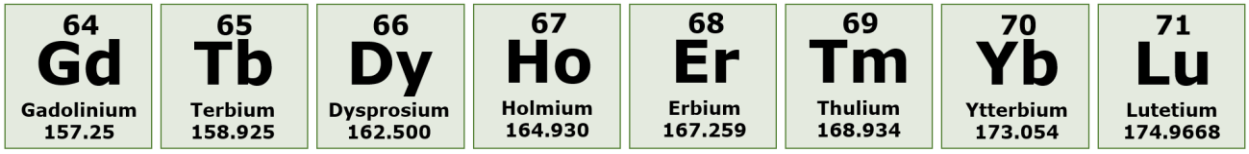

A logical substitution would be to stabilize Gd on the A site of the langasite lattice. This can be achieved by shrinking the overall size of the lattice. Attempts will be made to substitute Sc in

place of Ga. This substitution should, theoretically, shrink the lattice enough to accommodate Gd on the A site and maintain the langasite phase.

- Future directions for this research includes the synthesis of $2Gd_3Sc_3Ge_2BeO_{14}$

  $3Gd_2O_{3\,(s)} + 3Sc_2O_{3(s)} + 4GeO_{2(s)} + 2BeO_{(s)} \longrightarrow 2Gd_3Sc_3Ge_2BeO_{14\,(s)}$

- If successful, this will be expanded to accommodate Tb, Dy, Ho etc.

  For the already made langasites, attempts will be made to enhance the quality of the crystals and obtain a large single crystal. This will be done by attempting the growth in a four mirror furnace to ensure congruent melting and a very slow growth rate (0.1 mm/hr).

- Once the large single crystals are obtained, the directional dependence of the magnetic properties will be determined by aligning the crystals and performing the physical property measurements on them again.

- So far the MuSR measurements have only been obtained on $Nd_3Ga_3Ge_2BeO_{14}$, this will be expanded to the other members of the langasite family. The measurements will be performed at TRIUMF (Vancouver).

- Neutron scattering study of the langasites will also be expanded in the near future. Polarized neutron scattering will be performed on $Nd_3Ga_3Ge_2BeO_{14}$ at ILL at λ=1.8 Å.

- The diffuse scattering observed at the DCS for the Nd langasite will be further explored using CORELLI (Oak Ridge) as it offers high momentum resolution to easily separate Bragg peaks and diffuse scattering.

References

[1] J. S. Gardner, “Geometrically frustrated magnetism.,” *J. Phys. Condens. Matter*, vol. 23, no. 16, p. 160301, 2011.

[2] A. P. Ramirez, “Geometrical frustration,” *Handb. Magn. Mater.*, vol. 13, pp. 423–520, 2001.

[3] R. Moessner, A. P. Ramirez, R. Moessner, and A. P. Ramirez, “Geometrical Frustration,” *Phys. Today*, vol. 59, no. May 2013, 2006.

[4] C. Lacroix, “solid-state sciences,” in *Introduction ot Frustrated Magnetism*, New York: Springer, 2011, p. 500.

[5] J. E. Greedan, “Geometrically frustrated magnetic materials,” in *Functional Oxides*, 2001, pp. 50–75.

[6] L. Savary, “Quantum Spin Liquids,” Cambridge, 2016.

[7] L. Balents, “Spin liquids in frustrated magnets,” *Nature*, vol. 464, no. 7286, pp. 199–208, Mar. 2010.

[8] Y. J. Uemura, “Spin Fluctuations in Frustrated Kagome Lattice System SrcrsGa401y Studied by Muon Spin,” *PRL*, vol. 73, no. 24, pp. 10–13, 1994.

[9] M. Mekata, “Kagome: The Story of the Basketweave Lattice,” *Phys. Today*, vol. 56, no. 2, pp. 12–13, Feb. 2003.

[10] T.-H. Han, J. S. Helton, S. Chu, D. G. Nocera, J. A. Rodriguez-Rivera, C. Broholm, and Y. S. Lee, “Fractionalized excitations in the spin-liquid state of a kagome-lattice antiferromagnet,” *Nature*, vol. 492, no. 7429, pp. 406–410, Dec. 2012.

[11] S. Anthony, “MIT discovers a new state of matter, a new kind of magnetism,” *Extreme tech*, 2012. [Online]. Available: http://www.extremetech.com/extreme/143782-mit-discovers-a-new-state-of-matter-a-new-kind-of-magnetism.

[12] M. Punk, D. Chowdhury, and S. Sachdev, “Topological excitations and the dynamic structure factor of spin liquids on the kagome lattice,” *Nat Phys*, vol. 10, no. 4, pp. 289–293, Apr. 2014.

[13] Nishiyama. M., “Magnetic ordering and fluctuation in kagome lattice antiferromagnets, Fe and Cr jarosites,” Kyoto, 2000.

[14] F. Bert, P. Mendels, D. Bono, A. Olariu, F. Ladieu, J. C. Trombe, F. Duc, C. Baines, A. Amato, and A. Hillier, “Dynamics in pure and substituted volborthite kagome-like compounds,” *Phys. B Condens. Matter*, vol. 374–375, pp. 134–137, 2006.

[15] Gaulin, Bruce. "Frustrated Magnetism As Seen Through The Lens Of DCS". 2016. Presentation. *A Symposium Honoring John Copley, David Mildner and William Kamitakahara.* Accessed July 2016.

[16] A. Z. Sharma, H. J. Silverstein, A. M. Hallas, G. M. Luke, and C. R. Wiebe, "Structure and magnetic properties of new Be-substituted langasites A3Ga3Ge2BeO14 (A=Pr, Nd, and Sm)," *J. Solid State Chem.*, vol. 233, pp. 14–22, 2016.

[17] G. M. Kuzmicheva, E. N. Domoroschina, V. B. Rybakov, A. B. Dubovsky, and E. A. Tyunina, "A family of langasite: Growth and structure," *J. Cryst. Growth*, vol. 275, no. 1–2, pp. 715–719, 2005.

[18] H. J. Silverstein, K. Cruz-Kan, A. M. Hallas, H. D. Zhou, R. L. Donaberger, B. C. Hernden, M. Bieringer, E. S. Choi, J. M. Hwang, A. S. Wills, and C. R. Wiebe, "Pb3TeCo3V2O14: A Potential Multiferroic Co Bearing Member of the Dugganite Series," *Chem. Mater.*, vol. 24, no. 4, pp. 664–670, Feb. 2012.

[19] B. V Mill and M. V. L. Moscow, "Two New Lines of Langasite Family Compositions," in *IEEE International Frequency Control Symposium and PDA Exhibition TWO*, 2001, vol. 7803, no. 7, pp. 255–262.

[20] S. K. Pati and C. N. R. Rao, "Kagome network compounds and their novel magnetic properties," *Chem. Commun.*, no. 39, pp. 4683–4693, 2008.

[21] P. Bordet, I. Gelard, K. Marty, a Ibanez, J. Robert, V. Simonet, B. Canals, R. Ballou, and P. Lejay, "Magnetic frustration on a Kagomé lattice in $R_3Ga_5SiO_{14}$ langasites with R = Nd, Pr," *J. Phys. Condens. Matter*, vol. 18, no. 22, pp. 5147–5153, 2006.

[22] T. Kudo, Y. Yokota, M. Sato, K. Tota, K. Onodera, S. Kurosawa, K. Kamada, and A. Yoshikawa, "Growth of Al doped Ca3TaGa3Si2O14 piezoelectric single crystals with various Al concentrations," *J. Cryst. Growth*, vol. 401, pp. 173–176, 2014.

[23] A. Zorko, F. Bert, P. Mendels, K. Marty, and P. Bordet, "Ground State of the easy-axis rare-earth kagome langasite Pr3Ga5SiO14," *Phys. Rev. Lett.*, vol. 104, no. 5, pp. 3–6, 2010.

[24] A. Zorko, F. Bert, P. Mendels, A. Potočnik, A. Amato, C. Baines, K. Marty, P. Bordet, P. Lejay, E. Lhotel, V. Simonet, and R. Ballou, "Quantum Tunneling in Half-Integer-Spin Kagome-Lattice Langasites," *ArXiv Cond Matt*, vol. 14, pp. 1–7, 2012.

[25] K. Marty, "Etude des Langasites magnétiques De la frustration magnétique au multiferroïsme," Graduate Thesis, Néel Institut, Grenoble (France) 2008.

[26] J. Morton, "Types of Magnetism," in *Magnetic Properties of Materials*, 2012, pp. 1–50.

[27] Uiuc, "Four different kinds of magnetism," 2013. [Online]. Available: http://web.hep.uiuc.edu/home/serrede/P435/Lecture_Notes/Magnetism.pdf.

[28] N. Spaldin, *Magnetic Materials Fundamentals and applications*, Second. Santa Barbara: Cambridge, 2011.

[29] K. Seshan, *Handbook of Thin Film Deposition Processes and Techniques*. Elsevier, 2001.

[30] L. L. Hench and J. K. West, "The sol-gel process," *Chem. Rev.*, vol. 90, no. 1, pp. 33–72, Jan. 1990.

[31] T. Ahn, J. H. Kim, H.-M. Yang, J. W. Lee, and J.-D. Kim, "Formation Pathways of Magnetite Nanoparticles by Coprecipitation Method," *J. Phys. Chem. C*, vol. 116, no. 10, pp. 6069–6076, Mar. 2012.

[32] J. B. Wiley and R. B. Kaner, "Rapid solid-state precursor synthesis of materials.," *Science*, vol. 255, no. 5048, pp. 1093–1097, Feb. 1992.

[33] H. J. Kitchen, S. R. Vallance, J. L. Kennedy, N. Tapia-ruiz, L. Carassiti, A. Harrison, A. G. Whittaker, T. D. Drysdale, S. W. Kingman, and D. H. Gregory, "Modern Microwave Methods in Solid-State Inorganic Materials Chemistry : From Fundamentals to Manufacturing," *Chem. Rev.*, vol. 114, no. 1, pp. 1170–1206, 2014.

[34] A. Kopp Alves, C. P. Bergmann, and F. A. Berutti, "Combustion Synthesis," in *Novel Synthesis and Characterization of Nanostructured Materials*, 2nd ed., Heidelberg: Springer, 2013, p. 92.

[35] J. V Badding, "High-Pressure Synthesis, Characterization, And Tuning Of Solid State Materials," *Annu. Rev. Mater. Sci.*, vol. 28, no. 1, pp. 631–658, Aug. 1998.

[36] J. R. Creighton and P. Ho, "Chapter 1 Introduction to Chemical Vapor Deposition (CVD)," *Chem. Vap. Depos.*, vol. 6682, pp. 1–13, 2001.

[37] A. S. Sefat, "Flux Method for Preparing Crystals," Tennessee, 2010. http://www.icmr.ucsb.edu/programs/documents/Sefat1.pdf (May 2016)

[38] M. Ciomaga Hatnean, M. R. Lees, and G. Balakrishnan, "Growth of single-crystals of rare-earth zirconate pyrochlores," *J. Cryst. Growth*, vol. 418, pp. 1–6, 2015.

[39] A. Authier, *Early days of x-ray crystallography*, First. Oxford: Oxford University Press, 2013.

[40] Y. Waseda, E. Matsubara, and K. Shinoda, "Space groups," in *X-Ray Diffraction Crystallography*, 1st ed., New York: Springer, 2011.

[41] P. Hoffman, *Solid State Physics: An Introduction*, Second. Denmark: Wiley Publications, 2011.

[42] A. K. Cheetham and P. Day, *Solid State Chemistry Techniques*, First. New York: Oxford University Press, 1985.

[43] K. Ståhl, "Powder diffraction and the Rietveld Method,Technical University of Denmark" Lyngby, 2008. http://struktur.kemi.dtu.dk/kenny/Rietveld_Compendium.pdf (May 2016)

[44] M. Ladd and P. R, "Lattices and Space-Group Theory," in *Structure Determination by X-ray Crystallography: Analysis by X-rays and Neutrons*, 1st ed., New York: Springer Science, 2013, pp. 51–130.

[45] L. B. McCusker, R. B. Von Dreele, D. E. Cox, D. Louër, and P. Scardi, "Rietveld refinement guidelines," *J. Appl. Crystallogr.*, vol. 32, no. 1, pp. 36–50, 1999.

[46] R. A. Young and (Ed.), *The Rietveld Method*, 1st ed. New York: Oxford University Press, 1993.

[47] H. N. Nhat, "Bond valence calculation for several perovskites and the evidences for a valence charge transfer process in these compounds," Faculty of Physics, Hanoi University of Sciences, Hanoi, 2003.(https://arxiv.org/ftp/cond-mat/papers/0308/0308610.pdf) (June 2016)

[48] F. Li and X. Duan, "Applications of Layered Double Hydroxides," *Struct. Bond.*, vol. 119, no. September 2005, pp. 193–223, 2006.

[49] D. I. Brown, *Bond Valences*, First. New York: Springer, 2014.

[50] J. M. Vail, *Topics in theory of solid materials*, First. U.K.: Institute of Physics Publishing, 2003.

[51] H. D. Young, *Sears and Zemansky's University Physics*, 11th ed. New York: Benjamin-Cummings Pub Co, 2003.

[52] J. R. Hook and H. . Hall, *SOlid State Physics*, Second. New York: Wiley Publications, 2007.

[53] B. Luthi, "Crystal Field Effects In Rare Earth Systems," *J. Magn. Magn. Mater.*, vol. 15–18, pp. 1–8, 1980.

[54] C. Kittel, *Introduction to Solid State Physics*, Eighth. Berkeley, 2002.

[55] R.E. Taylor "Schottky systems" Thermal Expansion of Solids, ASM International First, Materials park, First edition pp-44-45 (1998)

[56] S. . Lee and S. . Kilcoyne, *Muon Science*, 1st ed. Scotland: Oxford University Press, 1998.

[57] A. J. Steele, "Quantum Magnetism Probed with Muon-SPin Relaxation," University of oxford, Graduate Thesis, 2011.

[58] M. Forker, "μ SR - Muon spin rotation , relaxation and resonance（ppt）," Vancouver, 2012. (http://mesonpi.cat.cbpf.br/e2012/arquivos/pg07/Chapter%205%20%C2%B5SR.pdf) (May 2016)

[59] A. Facure, A. X. Silva, R. C. Falc??o, and V. R. Crispim, "Neutron scattering in concrete and wood," *Radiat. Prot. Dosimetry*, vol. 119, no. 1–4, pp. 514–517, 2006.

[60] R. Pynn, "Neutron Scattering: A Primer," *Los Alamos Science*, vol. 19. p. 1, 1990.

[61] K. Lefmann, "Neutron Scattering: Theory, Instrumentation, and Simulation," University of Denmark, Graduate Thesis, 2007.

[62] R. Rinaldi and L. Liang, “Neutron Applications in Earth, Energy, and Environmental Sciences BT - Neutron Applications in Earth, Energy and Environmental Sciences,” 2009.

[63] S. Dekker, “Elastic And Quasielastic/ Inelastic Neutron Scattering,” Gaithersburg, 2008. https://www.ncnr.nist.gov/staff/hammouda/distance_learning/chapter_8.pdf

[64] W. Hill, BeO, “Safety Data Sheet,” Alfa Aesar, 2015.

[65] B. V. Mill, “Formation of phases with the Ca3Ga2Ge4O14 structure in the AO-TeO3-Ga2O3-XO2 (A = Pb, Ba, Sr; X = Si, Ge) and PbO-TeO3-MO-GeO2 (M = Zn, Co) systems,” *Russ. J. Inorg. Chem.*, vol. 55, no. 10, pp. 1611–1616, 2010.

[66] H. Guinier, “Guinier Camera G670,” 2010. [Online]. Available: http://www.xhuber.de/en/product-groups/2-applications/22-x-ray-cameras/guinier-g670/.

[67] G. Huber and G. Camera, “Monochromator 611 Manual,” PRIME Lab, 1st Ed. 2015.

[68] Physical Property Measurement System: Vibrating Sample Magnetometer (VSM)

Option Users Manual, Quantum Design Inc., San Diego, CA, 1st ed. (2004).

[69] P. Dalmas de Réotier, “Introduction to muon spin rotation and relaxation (μSR),” *CEA and University Joseph Fourier*, 2010. [Online]. Available: http://inac.cea.fr/Pisp/pierre.dalmas-de-reotier/introduction_muSR.pdf.

[70] J. Sonier, “Muon Spin Rotation/Relaxation/ Resonance (μSR),” μSr Studies Of Vortex State In Type-Ii Superconductors, Rev. Mod. Physics, 72, 769 (2000).

[71] J. R. D. Copley, “Time-of-flight spectroscopy and the Disk Chopper Spectrometer (DCS),” *NCNR Summer School 2011*, 2011. .

[72] J. R. D. Copley and J. C. Cook, “The Disk Chopper Spectrometer at NIST : a new instrument for quasielastic neutron scattering studies,” *Chem. Phys.*, vol. 292, pp. 477–485, 2003.

[73] ILL, “Time of Flight,” 2016. [Online]. Available: http://scalemodel.ill.fr/index.php?id=12593.(June 106)

[74] ILL, “ILL Instrument D7,” 2016. [Online]. Available: https://www.ill.eu/instruments-support/instruments-groups/instruments/d7/characteristics/.(June 2016)

[75] J. R. Stewart, P. P. Deen, K. H. Andersen, H. Schober, J. F. Barthélémy, J. M. Hillier, A. P. Murani, T. Hayes, and B. Lindenau, “Disordered materials studied using neutron polarization analysis on the multi-detector spectrometer, D7,” *J. Appl. Crystallogr.*, vol. 42, no. 1, pp. 69–84, 2009.

[76] B. V. Mill, “Langasites discovery to present.pdf,” in *IEEE/EIA International Frequency Control Symposium and Exhibition*, 2000, p. 4.

[77] Lumata L.L., “Low-temperature spin dynamics in the kagome system Pr3Ga5SiO14,” *Phys Rev B*, vol. 81, no. 224416, pp. 1–10, 2010.

[78] S. Ghosh, S. Datta, H. D. Zhou, M. J. R. Hoch, C. R. Wiebe, and S. O. Hill, “Electron Magnetic Resonance Studies of the Pr3Ga5SiO14 and Nd3Ga5SiO14 Kagomé Systems,” *J. Appl. Phys.*, vol. 109, no. 2011, p. 07E137(3), 2011.

[79] H. D. Zhou, C. R. Wiebe, Y. J. Jo, L. Balicas, R. R. Urbano, L. L. Lumata, J. S. Brooks, P. L. Kuhns, A. P. Reyes, Y. Qiu, J. R. D. Copley, and J. S. Gardner, “Chemical pressure induced spin freezing phase transition in kagome Pr langasites,” *Phys. Rev. Lett.*, vol. 102, no. 6, pp. 3–6, 2009.

[80] “Shannon Radii.” [Online]. Available: http://abulafia.mt.ic.ac.uk/shannon/ptable.php.

[81] H. D. Zhou, B. W. Vogt, J. A. Janik, Y. J. Jo, L. Balicas, Y. Qiu, J. R. D. Copley, J. S. Gardner, and C. R. Wiebe, “Partial field-induced magnetic order in the Spin-liquid kagom?? Nd3Ga5SiO14,” *Phys. Rev. Lett.*, vol. 99, no. 23, pp. 1–4, 2007.

[82] J. Rodríguez-carvajal, “Introduction to the Program FULLPROF,” Saclay, 2011.

[83] S. M. Deseller, “Magnetic Order and the Electronic Ground State in the Pyrochlore Iridate Nd2Ir2O7,” *Phys Rev B*, vol. 85, no. 174441, pp. 1–4, 2012.

[84] Q. J. Li, Z. Y. Zhao, H. D. Zhou, W. P. Ke, X. M. Wang, C. Fan, X. G. Liu, L. M. Chen, X. Zhao, and X. F. Sun, “Paramagnetic ground state with field-induced partial order in Nd 3Ga5SiO14 probed by low-temperature heat transport,” *Phys. Rev. B - Condens. Matter Mater. Phys.*, vol. 85, no. 17, pp. 3–8, 2012.

[85] R. Celotta, “Neutron Scattering,” in *Methods of Experimental Physics*, 1st ed., L. Marton, Ed. Orlando: Academic Press Inc., 1986.

[86] A. M. Hallas, A. M. Arevalo-Lopez, A. Z. Sharma, T. Munsie, J. P. Attfield, C. R. Wiebe, and G. M. Luke, “Magnetic frustration in lead pyrochlores,” *Phys. Rev. B*, vol. 91, no. 10, p. 104417, Mar. 2015.

[87] A. C. Anderson, “Calorimetric Investigation of the Hyperfine Interactions in Metallic Nd, Sm, and Dy,” *Phys Rev*, vol. 183, no. 546, 1969.

[88] A. Hallas, “Ho2Ge2O7 and Pr2Zr2O7: a tale of two spin ices,” *Master Thesis Univ. Manitoba*, 2013.

[89] I. Vishik, “What is the significance of the Schottky anomaly?,” 2014. [Online]. Available: https://www.quora.com/What-is-the-significance-of-the-Schottky-anomaly. [Accessed: 20-Jun-2003].

[90] Physical Property Measurement System: Image Furnace, Option Users Manual, Quantum Design Inc., San Diego, CA, 1st ed. (2004) [91]